This manuscript is a preprint and has not been peer reviewed. The copyright holder has made the manuscript available under a Creative Commons Attribution 4.0 International (CC BY) license and consented to have it forwarded to EarthArXiv for public posting.

Characterizing compound physical and biogeochemical extremes in the California Current Large Marine Ecosystem

Natalie M. Freeman[1*], Gaëlle Hervieux[1,2], Michael A. Alexander[1], Michael G. Jacox[1,3,4], Dillon J. Amaya[1], James D. Scott[1,2], Antonietta Capotondi[1,2],

1 NOAA Physical Sciences Laboratory, Boulder, CO, USA
2 Cooperative Institute for Research in Environmental Sciences, University of Colorado, Boulder, CO, USA
3 NOAA Southwest Fisheries Science Center, Monterey, CA, USA
4 University of California Santa Cruz, Santa Cruz, CA, USA

* natalie.freeman@noaa.gov

Abstract

Discrete environmental stressors, such as prolonged periods of extreme temperature or low oxygen, threaten the functioning of marine ecosystems. While considerable attention has been given to studying extremes occurring in isolation, our understanding of such events co-occurring in the water column–referred to as multi-stressor events or compound extremes–is still limited, despite their potentially synergistic effects on individual species. We use a historical ocean model simulation with biogeochemistry to characterize the frequency, intensity, and duration of multi-stressor events (temperature, chlorophyll, and oxygen) in the California Current Large Marine Ecosystem (CCLME) from 1996–2019. We highlight key spatiotemporal patterns of compound physical and biogeochemical extremes in the context of large-scale climate variability, particularly ENSO. Marine heatwaves and low chlorophyll extremes are generally associated with strong El Niño events, while shallow hypoxia extremes are generally associated with La Niña events. Marine heatwave-low chlorophyll extremes are the most common compound extreme in nearshore waters, while triple extremes are relatively rare, as conditions favoring warm and low productivity anomalies tend to also favor high oxygen anomalies. Results from this study advance our understanding of where and when multi-stressor events tend to occur in the CCLME, highlighting spatiotemporal characteristics that suggest potential sources of predictability, which could be leveraged in the ecosystem-based management of living marine resources.

1 Introduction

The California Current Large Marine Ecosystem (CCLME; Fig 1) is one of the world's most biologically productive ocean regions (e.g., [1]). Wind-driven upwelling in the California Current System (CCS) supplies nutrient-rich waters to the upper ocean, fueling primary production that supports a diversity of marine species. The management of commercial and recreational fisheries, as well as marine protected areas, supports local economies, communities, and cultures. It is therefore of great interest to scientists, managers, and stakeholders to understand not only the dynamics of the CCLME but its vulnerabilities through targeted research into the fundamental physical processes that characterize it.

Ecosystem stressors, and in particular, discrete periods of extreme environmental conditions have the potential for sudden and/or outsized impacts on the physiology, behavior, and mortality

This manuscript is a preprint and has not been peer reviewed. The copyright holder has made the manuscript available under a Creative Commons Attribution 4.0 International (CC BY) license and consented to have it forwarded to EarthArXiv for public posting.

Fig 1. The study region. Geographic region making up the California Current Large Marine Ecosystem (dark green contour). The nearshore coastal band (within 0–75 km of the coast) is divided into zones 1–4 (shades of brown) and the offshore coastal band (within 75–300 km of land) is divided into zones 5–8 (shades of blue).

of marine species. Spurred largely by several recent periods of extremely warm ocean temperatures–known as marine heatwaves (MHWs)–considerable attention has been given to improving our understanding of these extremes (e.g., [2]), including their physical drivers (e.g., [3–5]), predictability (e.g., [6, 7]) and ecosystem-wide impacts (see [8] and references therein). For example, the 2013-2015 Northeast Pacific Warm "Blob" saw devastating impacts along the North American west coast, with extensive ecological and socioeconomic consequences, such as outbreaks of toxic algae and the closure of commercially important fisheries (e.g., [9, 10]). In contrast, the study of extremes in other ecosystem-relevant variables, such as oxygen, pH, or chlorophyll is relatively limited despite recognition of their ecological importance (see [11]). For example, chlorophyll is a proxy for phytoplankton biomass and has been shown to be a useful indicator of fisheries yields [12]. Biogeochemical extremes such as hypoxia (low oxygen) or acidification (low pH) events have plagued the Pacific Northwest shellfish industry, causing mass die-offs [13] and hatchery failures (Barton et al., 2015), respectively. Such impacts have further galvanized the fisheries industry to seek scientific collaboration to inform adaptation strategies for more resilient operations (e.g., see [14]).

Indeed, the direct impacts of marine heatwaves occurring in isolation are relatively well-documented (e.g., [9]) compared to the marine ecosystem and biodiversity impacts of two or more extremes, or "compound events" (see [15]). The synergistic effects of co-occurring high temperature-low chlorophyll or high temperature-low oxygen extremes are of particular concern, as elevated temperatures increase organismal metabolic requirements (e.g., [16]), effectively lowering hypoxia tolerances and raising feeding demands. The recent collapse of the Bering Sea snow crab is a prime example, where a combination of high metabolism and low food supply was linked to mass mortality and fishery closure between 2018 and 2022 [17]. Lucey et al. [18] showed that in the case of a tropical sea urchin, mortality increased upon exposure to a compound MHW-low oxygen event, compared to a MHW or hypoxic event alone. Murie and Bourdeau [19] demonstrated that species-specific responses to single extremes are insufficient predictors of responses to multiple stressors (e.g., warming, hypoxia), highlighting the importance of increasing our understanding of the combined and cascading effects of multi-stressor extremes on coastal ecosystems.

Extreme events can also compress or displace species' preferred habitat (e.g., [20, 21]), with implications for ecosystem dynamics (e.g., predator-prey relationships, carbon export) and resource management (e.g., shifting species' distributions, increased bycatch potential). For marine species with little to no mobility (e.g., oyster reefs, crabs), single and compound extremes can be devastating. While there are some highly mobile species that can relocate in order to maintain their preferred habitat (e.g., [22]; see discussion in [23]), even the day-to-day vertical movements of some species can be impacted by a multivariate compound extreme in the water column. For example, Iglesias et al. [24] demonstrated that compound MHW-low chlorophyll conditions can indirectly alter (i.e., deepen) the vertical distribution of mesopelagic fish in the central CCS by increasing the amount of light that can penetrate mesopelagic depths, with implications for total energy expenditure by their predators (e.g., seals) forced to forage longer and deeper in the water column.

The CCLME is governed by atmospheric and oceanic forcing of remote and local origin on daily-to-decadal timescales, largely through the modulation of upwelling and mixing, influencing temperature, stratification, nutrient and oxygen availability, and biological productivity (e.g., [25]). For instance, the dynamics of short- and long-lived mesoscale features, such as eddies, fronts, and upwelling can shape local biodiversity patterns on daily-to-seasonal timescales, influencing productivity and aggregating prey and their predators [26, 27]. On

This manuscript is a preprint and has not been peer reviewed. The copyright holder has made the manuscript available under a Creative Commons Attribution 4.0 International (CC BY) license and consented to have it forwarded to EarthArXiv for public posting.

interannual timescales, the predominant driver of CCS variability is the El Niño-Southern Oscillation (ENSO) via atmospheric teleconnections (e.g., the atmospheric bridge; [28, 29]) and oceanic processes (e.g., coastally trapped waves (CTWs); [30]). For example, downwelling CTWs were observed during the 1997–1998 El Niño, deepening the thermocline along their path and helping to drive widespread bottom MHWs (BMHWs) along the continental shelves [31, 32], with implications for benthic habitats, kelp forests, fish populations, and commercial fisheries. On multi-year to decadal timescales, basin-scale variability associated with the Pacific Decadal Oscillation (PDO; [33, 34]) and North Pacific Gyre Oscillation (NPGO; [35]) can drive distinct long-term responses in upwelling along the west coast, and thus, marine biota. For example, the NPGO has been found to be significantly correlated with variability in salinity, nutrients, and chlorophyll concentration off California (see [36] and references therein). In addition to natural climate variability, long-term ocean warming [37], deoxygenation [38, 39], and acidification [40] threaten to disrupt the structuring of marine ecosystems.

In this study, we evaluate oceanic extremes in temperature, chlorophyll, and hypoxic layer depth and characterize their spatiotemporal distribution and compound prevalence within the CCLME using a historical (1996–2019) ocean hindcast with biogeochemistry. Additionally, we discuss these oceanic extremes against the backdrop of large-scale climate variability, including strong El Niño and La Niña events over the study period. Our overall aim is to expand our understanding of physical and biogeochemical extremes in the CCLME, highlighting where and when certain regions are most susceptible to single and compound extremes.

2 Data and methods

2.1 Study region

The CCLME spans the western North American coast between 22–48°N, extending as far west as 132°W (Fig 1). For this study, we define two cross-shore bands within the CCLME, referred to as "nearshore" and "offshore," defined to be within 0–75 km and 75–300 km of land, respectively. We further divide each of these bands into four alongshore zones, with delineation from north to south at 40°N, 35°N, and 30°N. We present analyses of the CCLME, its nearshore and offshore bands, as well as their eight zones, as area-weighted, regional averages. We also define boreal winter as January-February-March (JFM), spring as April-May-June (AMJ), summer as July-August-September (JAS), and fall as October-November-December (OND).

2.2 Global ocean hindcast with biogeochemistry

We evaluate output from a global ocean biogeochemical hindcast simulation (FREEBIORYS2V4; https://doi.org/10.48670/moi-00019) made available through the Copernicus Marine Environmental Monitoring Service (CMEMS). The PISCES-v2 (Pelagic Interactions Scheme for Carbon and Ecosystem Studies) biogeochemical ocean model [41] is initialized with global distributions of nutrients and dissolved oxygen from the World Ocean Atlas 2013 climatology [42] and forced offline by daily mean fields of atmospheric conditions from the European Center for Medium-Range Weather Forecasts (ECMWF) ERA-Interim atmospheric reanalysis [43] and physical ocean and sea ice conditions obtained from the Mercator-Ocean FREEGLORYS2V4 numerical simulation (see extensive descriptions in [44] and [45]). Bicubic interpolation was used to map the FREEGLORYS2V4 output onto the FREEBIORYS2V4 grid. These data, hereafter referred to as GLORYS-BGC, consist of daily or monthly mean physical and biogeochemical ocean variables from 1993-2019 at 0.25 degree ($\sim$25 km) horizontal resolution and 75 vertical levels [46]. We limit our study of extremes to years 1996–2019 for which model values are realistic for the region and exhibit no apparent drift (not shown). To standardize the temporal resolution across years, all leap day entries (February 29) were excluded from the dataset.

This manuscript is a preprint and has not been peer reviewed. The copyright holder has made the manuscript available under a Creative Commons Attribution 4.0 International (CC BY) license and consented to have it forwarded to EarthArXiv for public posting.

2.3 Detection of extreme events

In this study, we define extremes of temperature, chlorophyll, and hypoxic layer depth (HLD) as a MHW, low chlorophyll extreme (LCX), and shallow hypoxia extreme (SHX), respectively (Table 1). Prior to event detection, we define a bulk chlorophyll concentration by vertically-integrating the upper 100 m chlorophyll concentration ($\int$Chl; $mg\ m^{-2}$). Dissolved oxygen concentration is linearly interpolated in the vertical prior to defining the HLD (m) as the shallowest 2 $mg\ L^{-1}$ oxygen isopleth (2 $mg\ L^{-1} \simeq 62.5\ mmol\ m^{-3}$ using a molar weight of 31.998 $g\ mol^{-1}$). As such, both chlorophyll and oxygen-related extremes are defined using a single value while still representing a water column extreme with relevance to ecosystem dynamics. While we assess MHWs throughout the water column, we have chosen to present results largely focused on surface-defined MHWs (SMHWs) across the CCLME, and, given their implications for benthic and demersal species, bottom MHWs occurring along the seafloor of the nearshore region (see [32]). In the latter case, we isolate bottom temperatures only at locations where the ocean bottom is shallower than 1000 m. Trends in temperature, $\int$Chl, and HLD were assessed but not removed prior to event detection, given the relatively short study period and consistent with recent studies of extremes (e.g., [47]); a sensitivity analysis on detrended data shows no significant change in the results presented here (not shown).

Table 1. Percentile (P) thresholds and naming conventions used to define extreme events.

	Temperature		$\int$Chl		HLD	
Percentile threshold	$< P10$	$> P90$	$< P10$	$> P90$	$< P10$	$> P90$
Extreme event name	*marine cold spell*	*marine heatwave*	*low chlorophyll extreme*	*high chlorophyll extreme*	*shallow hypoxia extreme*	*deep hypoxia extreme*
Extreme event acronym	MCS	MHW	LCX	HCX	SHX	DHX

From the model grid cell level to the regional level, single and compound (double and triple) extremes are detected over a given time period using a seasonally-varying relative threshold approach with an 11-day window size centered on the day of the year and extended over the 24 year record (as in [48]). In the case of a MHW, we define an extreme temperature event as any $\geq$ 5 day period exceeding the 90th percentile (P90; Table 1; [49]). For LCX and SHX, any $\geq$ 5 day period below the 10th percentile (P10) is considered an extreme event (Table 1; [47]). In the latter case, a SHX indicates a persistent, extreme shoaling of the HLD (similar to the THREEs metric used by [50]). If any consecutive extreme events occur $\leq$ 3 days apart, the events are combined and counted as a single event. Any time periods where two or more events co-occur in the water column for at least 5 days are deemed compound extreme events (e.g., Fig 2) illustrates a single day of a triple extreme as defined in this study).

Fig 2. Example of a triple extreme in the water column. Snapshot of the upper 370 m water column on May 4, 2005 during a triple extreme event identified off the southwest coast of Oregon (43.25°N, 125°W) that began on May 4 and ended on May 8. The solid contours represent the daily (May 4) climatological mean vertical profiles of temperature (orange) and chlorophyll (green) and dissolved oxygen (blue) concentration. The corresponding dashed contours indicate the instantaneous or extreme profile of these properties when a concurrent SMHW (P90 = 13.1°C), LCX (P10 = 31.7 $mg\ m^{-2}$), and SHX (P10 = 159.6 m) was identified on May 4, 2005. The climatological (solid green bracket) and instantaneous (dashed green bracket) vertically-integrated (0–100 m; light green shading) chlorophyll concentration values are annotated. Waters below the HLD (blue stars) are hypoxic (light blue shading); the carrot along the x-axis of dissolved oxygen marks the hypoxia threshold of 62.5 $mmol\ m^{-3}$.

This manuscript is a preprint and has not been peer reviewed. The copyright holder has made the manuscript available under a Creative Commons Attribution 4.0 International (CC BY) license and consented to have it forwarded to EarthArXiv for public posting.

It is common to define hypoxia using a threshold of 2 $mg\ L^{-1}$, a cutoff conventionally used in fisheries management decisions, despite some species having lower or higher tolerances (see [51] and references therein). Our choice to define oxygen-related events based on extreme vertical displacements of the HLD is robust for a variety of hypoxic thresholds (1.5 and 4 $mg\ L^{-1}$) and less sensitive to model biases in absolute oxygen concentration (not shown). In shallower water columns along the continental shelf, the absence of an HLD is not uncommon, as the presence of hypoxia can vary by location and season (e.g., see [22]), with approximately 30% of the GLORYS-BGC nearshore domain experiencing some form of this. For nearshore assessments, undefined HLDs are treated as NaNs prior to calculating the spatially-weighted median, limiting contributions to areas where hypoxia is present and helping minimize seasonal biases. For pointwise calculations used to describe SHXs–including both the climatology and percentile threshold–we instead replace an undefined HLD with the ocean bottom depth at that location, effectively representing a fully oxygenated water column ("no hypoxia"). Such instances are not considered valid extreme days and are excluded from SHX event identification. A sensitivity test in which undefined HLDs are retained as NaNs (not shown) yields generally shallower threshold values, effectively imposing a stricter event criterion and resulting in modest changes in pointwise SHX frequency, intensity, and duration along the shelf.

2.4 Characterization of extreme events

Extreme events are characterized by three metrics: duration, intensity, and frequency. Duration is defined as the number of days an event remains above or below its respective percentile threshold, and intensity as the average anomaly over that period. For compound events, duration is the length of time over which the univariate extremes occur, and intensity is the product of their standardized anomalies or z-scores (Z; as in [52] and [53]; see Section 2.8 for the computation of the geometric z-score for chlorophyll). Our analysis assumes that both positive and negative anomalies reflect departures from typical conditions that contribute to ecological stress, with the multiplication of z-scores ensuring positive compound intensities when extremes align in stress-associated directions.

For example, for a given location, the intensity (Ψ) of compound MHW-SHXs over the study period is expressed as

$$\Psi = Z_{MHW} \times Z_{SHX},$$

which is then standardized by subtracting the temporal mean (μ_Ψ) and dividing by the temporal standard deviation (σ_Ψ):

$$\Psi' = \frac{\Psi - \mu_\Psi}{\sigma_\Psi},$$

This final standardization ensures comparability across compound event types by transforming intensities into a common z-score scale, enabling direct comparison of event anomalies relative to typical behavior. In addition to the product of z-scores method, computing compound event intensities (Ψ) using the Euclidean norm approach (as in [54]) yields consistent results, with key takeaways remaining unchanged across both methods (not shown).

The frequency of a single or compound event is the number of times it occurs within a given temporal range. For example, the triple extreme event present on May 4, 2005 at 45°N and 235°E off Oregon (Fig 2) included a surface MHW (SMHW) with an SST value (13.4°C) exceeding the 90th percentile (13.1°C) of all SST values simulated between April 29 and May 9 (11-day window) across all 24 years (264 total seasonally-independent SST values). This particular SMHW is characterized by a mean intensity of 1.2°C (1.35σ) and a duration of seven days (May 2–May 8), occurring in a location that has seen 38 SMHWs over the study period (i.e., a frequency of 1.58 events per year; not shown).

This manuscript is a preprint and has not been peer reviewed. The copyright holder has made the manuscript available under a Creative Commons Attribution 4.0 International (CC BY) license and consented to have it forwarded to EarthArXiv for public posting.

2.5 Observations

We use daily SST values from the NOAA Optimum Interpolation Sea Surface Temperature (OISSTv2) blended satellite product available on a 0.25 degree grid [55, 56]. Satellite estimates of surface chlorophyll concentration are provided by the European Space Agency Climate Change Initiative (ESA-CCI) as a blended 4 km product (version 6; [57]). Prior to analysis, we regrid the satellite-derived SST and chlorophyll products onto the standard 0.25 degree GLORYS-BGC grid using inverse distance weighting based on the four nearest neighbors. We then mask the model output according to the temporal availability of satellite retrievals.

We also employ in situ observations collected seasonally through the California Cooperative Oceanic Fisheries Investigations (CalCOFI; [38]) sampling program along lines 76.7, 80, 83.3, 86.7, 90, and 93.3 (see map in S2 Fig). In accordance with CalCOFI quality control procedures, data flagged as suspect or otherwise unreliable were excluded from analysis, though the removal of individual oxygen samples does not result in undefined HLDs at that location, as sufficient remaining samples in the vertical profile allow for the calculation of the HLD. We subsample GLORYS-BGC in time (day) and space (latitude, longitude, depth) using nearest neighbor interpolation to match CalCOFI observations between January 1996 and December 2019. We quantify the modeled and observed bulk chlorophyll concentration by vertically integrating over the upper 100 m of available samples ($\int$Chl); we also vertically interpolate oxygen concentration prior to defining the HLD. Then, we spatially average both modeled and observed CalCOFI data into nearshore and offshore cross-shore bands for direct comparison and compute seasonal averages.

2.6 Hindcast evaluation

GLORYS-BGC has been previously validated against observational products [44] and utilized in studies of MHWs [58], low oxygen extremes [59], MHW-LCX compound extremes [53], ENSO-driven variability in Eastern Boundary Upwelling Systems [60], biogeochemistry along Lagrangian pathways [45, 61], and as environmental context to observational sampling expeditions [62]. To assess the ability of the GLORYS-BGC hindcast to represent realistic extreme relationships in the CCLME, we leverage a combination of satellite products and ship-based observations of surface and subsurface temperature and chlorophyll concentration, as well as ship-derived HLD in this region over the last two decades.

We use satellite estimates of surface ocean properties to assess the model's ability to reproduce historical extreme events, defining a probability of detection (POD) as the percentage of observed extremes correctly simulated by the model:

$$\text{POD} = \frac{h}{h+m} \times 100,$$

where h is the number of observed extreme events that the model correctly simulates ("hits") and m is the number of observed extreme events that the model fails to simulate ("misses"). In the case of CCLME SMHWs, GLORYS-BGC has a POD of 82% when compared with OISSTv2 over the 1996–2019 period (S1 Fig). Geographically, we find the highest POD values in the CCLME north of 30°N as well as the nearshore region of the central Baja California Peninsula (hereafter referred to as Baja; S1 Fig). The lowest POD values are found in the Southern California Bight, where values drop below 40% (S1 Fig), suggesting that GLORYS-BGC has some difficulty simulating MHW dynamics in this highly variable region of the CCS. While OISSTv2 is a blended observational product, including cloud-penetrable microwave SST retrievals, sparse availability of visible light-reliant ESA-CCI chlorophyll retrievals precludes a robust POD analysis for low surface chlorophyll extremes (not shown). In the portions of the CCLME where at least 50% of a given season is available, we can partially evaluate regional seasonal mean biases. Indeed, we find that the model tends to overestimate seasonal surface chlorophyll concentration in the nearshore north of ~28°N ($< 0.7\sigma$) and underestimate it south

This manuscript is a preprint and has not been peer reviewed. The copyright holder has made the manuscript available under a Creative Commons Attribution 4.0 International (CC BY) license and consented to have it forwarded to EarthArXiv for public posting.

of ∼28°N (> -0.7σ) throughout the year (not shown). However, we note that event detection is not influenced by seasonal mean biases when using a seasonally-varying relative threshold approach.

Using in situ observations from the CalCOFI program, we evaluate the GLORYS-BGC hindcast's ability to reproduce observed variance and covariance among extreme variables. In the nearshore CalCOFI region, modeled relationships between environmental stressors align well with those observed, while offshore agreement is somewhat weaker, particularly for hypoxic layer depth (HLD) relationships (S2 Fig). Across both regions, warm surface temperature anomalies are generally associated with low $\int$Chl anomalies, and vice versa. This inverse SST–$\int$Chl relationship is the strongest among the three variables and is most accurately captured by the model, as indicated by higher correlation coefficients and narrow, elongated confidence ellipses. By contrast, relationships involving HLD are weaker and more variable. Deep HLD anomalies show only modest correlation with warm SST and low $\int$Chl anomalies, as evidenced by lower correlation coefficients and broader, more circular ellipses—likely reflecting the more complex biogeochemical and physical drivers of dissolved oxygen variability (see [63]).

We further evaluate the correlation between observed and modeled anomalies (S3 Fig), with attention to variability associated with ENSO. During strong ENSO events, the model reasonably captures the expected anomaly signatures for warm and cold phases. For instance, during the 1997–1998 El Niño, GLORYS-BGC successfully reproduces the anomalously warm nearshore SSTs, low $\int$Chl, and deep HLDs observed in CalCOFI records, in line with our broader findings on compound extremes presented in subsequent sections (S3 Fig; [64]). These results provide confidence in the ability of GLORYS-BGC to capture the relevant physical–biogeochemical relationships that underpin compound extremes in this region.

2.7 Climate and upwelling indices

Throughout this study, we discuss multi-stressor extremes in the context of local and remote forcing on seasonal-to-decadal timescales, employing various climate indices describing ENSO, PDO, NPGO, and coastal upwelling. ENSO is described by the Niño 3.4 index, which is defined as the area-averaged sea surface temperature (SST) anomaly over 5°S–5°N, 170–120°W (see https://www.cpc.ncep.noaa.gov/data/indices/). The PDO index [65] is defined as the leading Principal Component of North Pacific SST anomalies (north of 20°N), obtained by removing both the climatological annual cycle and the global average SST. The NPGO index is defined as the second Principal Component of monthly sea surface height (SSH) anomalies (SSHa; [35]) in the Northeast Pacific region (180–110°W; 25–62°N). The Coastal Upwelling Transport Index (CUTI; [66]) is an estimate of the total vertical transport through the base of the mixed layer and is derived from SSH, mixed layer depth (MLD), and surface wind stress (τ); here, MLD is computed using a density threshold criterion; specifically, the MLD is the depth at which the density of the water column differs from the 10 m density by a value of 0.125 $kg\ m^{-3}$, suitable for analyses focused on monthly and interannual timescales (e.g., [67]). All indices are computed using the common climatological reference period (January 1996–December 2019) and calculated as detailed above using monthly SST, SSH, MLD, and τ from GLORYS-BGC; model Niño 3.4, PDO, and NPGO indices compare well with observed indices, with correlation coefficients exceeding 95% (not shown).

2.8 Statistical approach

Mean values reported for a given region are computed as area-weighted averages. Anomalies are expressed as the difference between the period of interest and a given reference climatology. To facilitate comparison across variables, anomalies are standardized by dividing by the reference period standard deviation, yielding z-scores–anomalies expressed in units of standard deviation (σ). Given that chlorophyll and net primary production are log-normally distributed, we

This manuscript is a preprint and has not been peer reviewed. The copyright holder has made the manuscript available under a Creative Commons Attribution 4.0 International (CC BY) license and consented to have it forwarded to EarthArXiv for public posting.

compute statistics in space and time using the geometric mean (μ_g), standard deviation (σ_g), and standardized anomaly (z-score; Z_g) as

$$\mu_{\mathrm{g}} = e^{\frac{1}{n}\sum_{i=1}^{n} ln(x_i)},$$

$$\sigma_{\mathrm{g}} = e^{\sqrt{\frac{1}{n}\sum_{i=1}^{n} ln(\frac{x_i}{\mu_g})^2}},$$

$$\mathrm{Z}_{\mathrm{g}} = \frac{ln(\frac{x}{\mu_g})}{ln(\sigma_g)},$$

respectively, where n corresponds to the total number of samples (i) of a property (x) in a given time or space bin.

As in Le Grix et al. [47], the likelihood multiplication factor (LMF) is computed as the ratio of the observed joint frequency of all N $\geq$ 2 individual extremes occurring simultaneously (i.e., the compound event) to the product of their marginal frequencies ($f(E_i)$; [68]):

$$\mathrm{LMF} = \frac{f(E_1 \cap E_2 \cap \ldots \cap E_n)}{\prod_{i=1}^{n} f(E_i)}.$$

For example, we would theoretically expect independent MHW-SHX events to occur 1% of the time (10% $\times$ 10%), by definition. However, effective percentile thresholds can be reduced after applying additional criteria such as a 5-day minimum duration, resulting in lower marginal frequencies due to the exclusion of shorter (1–4 day) events. As such, all frequencies used in the LMF calculation reflect the filtered definition of extremes. An LMF greater than 1 indicates that compound events occur more frequently than would be expected by chance (i.e., positive statistical dependence), suggesting shared drivers or physically coupled processes. Conversely, an LMF less than 1 suggests negative dependence or mutual exclusion, where the events co-occur less often than expected under independence, potentially reflecting competing or uncoupled physical mechanisms.

3 Results

3.1 Characteristics of single and compound extremes and their spatial variability

We find that single and compound extremes in SST, $\int$Chl, and HLD exhibit distinct spatial patterns in mean frequency, intensity, and duration across the CCLME. SMHWs are frequently detected throughout the LME, with much of the region experiencing a consistent number of events exhibiting similar mean intensity and duration (Fig 3). In contrast, the highest occurrence of LCXs and SHXs is generally concentrated near the coast. LCXs are particularly frequent, with the most events found north of San Francisco Bay. Nearshore LCXs tend to be relatively weak and short-lived, except in zone 1 off Baja where durations can exceed 200 days (Figs 3 and 4). This pattern largely reflects the background mean and temporal variability of chlorophyll concentration in this region: where mean $\int$Chl is high and variability is frequent, more short-duration extremes are identified, and vice versa (Fig 3). In the case of SHXs, we find the most intense (up to 5σ; Fig 4) but relatively short-lived (<50 days; Fig 4) events throughout the nearshore (Figs 3 and 4). For example, off the Pacific Northwest coast (PNW; zone 4 latitudes), we find the strongest but shortest-lived SHXs along the shelf (Figs 3 and 4), consistent with Damien et al. [69] as a ‘hypoxia hotspot.’ In contrast, the Southern California Bight (SCB; zone 2 latitudes) stands out as a nearshore exception, where on average, relatively long-lasting (>200 days) but weak (<1.5σ) and infrequent SHXs occur (Figs 3 and 4). The longest-lasting

This manuscript is a preprint and has not been peer reviewed. The copyright holder has made the manuscript available under a Creative Commons Attribution 4.0 International (CC BY) license and consented to have it forwarded to EarthArXiv for public posting.

Fig 3. Maps of single extreme characteristics over the study period (1996–2019). Frequency (top row), mean intensity (middle row; mean z-score (Z), expressed in sigma units), and mean duration (bottom row; days) of SMHWs (left column), LCXs (middle column), and SHXs (right column). The black contour marks the boundary of the CCLME.

Fig 4. Intensity–duration–frequency relationships for single extreme events across zones. Single extremes of SMHWs (browns; left), LCXs (greens; middle), and SHXs (purples; right) are binned by duration (x-axis; days), intensity (y-axis; z-score (Z), expressed in sigma units), and frequency (color; average number of events per year) from 1996 to 2019. Markers (open circles) are overlain to represent the median of the distribution. Each extreme displays the nearshore zones 1–4 on the right and offshore zones 5–8 on the left, just as they appear in Fig 1 (zone numbers increase from south to north). Note, colorbar ranges differ between extremes.

events–whether single or compound–tend to occur far offshore (>300 km from the coastline), in open ocean areas characterized by low productivity and species diversity relative to the continental shelf and slope (Figs 3 and 5).

The compound events with the largest spatial footprint in the CCLME from highest to lowest are SMHW-LCXs, SMHW-SHXs, LCX-SHXs, and SMHW-LCX-SHXs (Fig 5), with triple extremes having only occurred over less than 23% of the LME between 1996 and 2019. The most intense (in a standardized sense) and longest-lasting SMHW-LCXs tend to occur far offshore (>300 km from the coast), though at a lower mean frequency than nearshore events (Fig 5). In contrast, the most recurrent SMHW-LCXs are found along the coast, with highest frequency values (>1 event per year) stretching across the majority of the LME coastline, from ∼27–45°N (Fig 5). Coastal SMHW-LCXs occurring south of Point Conception (∼35°N; Fig 5; zones 1–2 and 5–6; Fig 6) generally last longer than those to its north (zones 3–4 and 7–8; Fig 6). Notably, a large portion of the Baja coastline (within ∼300 km) spent the highest number of days (up to 620 days or ∼7% of total days) over the 24 year study period in SMHW-LCX status (see Section 3.2).

Fig 5. Maps of compound extreme characteristics over the study period (1996-2019). Frequency (top row), mean intensity (middle row; Ψ', expressed in sigma units), and mean duration (bottom row) of compound SMHW-LCX (first column), LCX-SHX (second column), SMHW-SHX (third column), and SMHW-LCX-SHX (fourth column). The black contour marks the boundary of the CCLME.

Fig 6. Intensity–duration–frequency relationships for compound extreme events across zones. Compound extremes of SMHW-LCXs (oranges; left), LCX-SHXs (greens; second from left), SMHW-SHXs (pinks; second from right), and SMHW-LCX-SHXs (grays; right) are binned by duration (x-axis; days), intensity (y-axis; Ψ', expressed in sigma units), and frequency (color; number of events per year) from 1996 to 2019. Markers (open circles) are overlain to represent the median of the distribution. Each extreme displays the nearshore zones 1–4 on the right and offshore zones 5–8 on the left, just as they appear in Fig 1 (zone numbers increase from south to north). Note, colorbar ranges differ between extremes and the LCX-SHX y-axis has been restricted to display the most common range across extremes, hiding an outlier event found in the 9.75–10σ intensity and 5–7 day duration bin.

Unlike SMHW-LCXs, LCX-SHXs do not occur everywhere in the CCLME, with the least number of events in zone 1 off Baja (Figs 5 and 6). Where LCX-SHXs do occur in the nearshore and offshore bands, they are relatively short-lived (Figs 5 and 6). For example, off the coast of northern California in zone 7, we find elevated occurrences of this particular compound biogeochemical extreme, where the median event exhibits a 2.3σ standardized intensity and

This manuscript is a preprint and has not been peer reviewed. The copyright holder has made the manuscript available under a Creative Commons Attribution 4.0 International (CC BY) license and consented to have it forwarded to EarthArXiv for public posting.

14-day duration (Figs 5 and 6). While SMHW-SHXs are generally more prevalent across the CCLME than LCX-SHXs, large portions of the nearshore band off California and Baja do not experience any SMHW-SHXs (Figs 5 and 6). In the coastal region, the rarity of SMHW-SHX events is consistent with upwelling dynamics that couple low oxygen to low temperatures. At these nearshore locations, SMHW-SHXs that do occur are relatively short-lived and likely a result of independent processes, which we discuss in the following section (Section 3.2). Outside of the nearshore, SMHW-SHX intensity appears generally correlated with duration, where relatively strong events are also long-lived, and vice versa (Figs 5 and 6). The opposite relationship generally holds true in the case of triple extremes: while SMHW-LCX-SHXs across the CCLME are generally strong ($>2\sigma$), they are also infrequent (<0.3 per year or <7 events total, approximately) and short-lived (Fig 5). Off the coast of northern California in zone 7, median triple event (standardized) intensity and duration is 3.6σ and 19 days, respectively (Fig 6). Triple extremes are a relatively rare occurrence in general, as there are more triple extreme-free areas in the CCLME than not, particularly in the nearshore (Figs 5 and 6).

3.2 The most common compound extremes in the CCLME

Based on total days over the study period, we find that SMHW-LCXs are the most commonly occurring compound extreme conditions in the CCLME (Fig 7). The nearshore in particular is most often experiencing SMHW-LCX conditions (Fig 7), with the total number of extreme days (1996–2019) generally increasing southward along the coast, from $\sim$100 days off Washington and northern Oregon to more than 500 days off portions of Baja (S4 Fig). The modeled frequency of SMHW-LCXs (Fig 5) across the region reflects largely positive LMF values (see Section 2.8), with the highest values occurring near the coast (S5 Fig). The positive LMF values indicate a positive correlation between SMHWs and LCXs, such that SMHW-LCXs occur more frequently than by chance. For example, SMHW-LCXs are more than five times more likely to occur along the California and Baja coasts than expected, while LCX-SHXs and SMHW-SHXs tend to occur at a reduced likelihood (LMF$<$1) in the nearshore (S5 Fig), suggesting a negative correlation between their component events (i.e., when an LCX is present in the water column, it is less likely that an SHX is also present). In the case of nearshore LCX-SHXs, the processes that drive a SHX (e.g., coastal upwelling) would also tend to stimulate phytoplankton growth (e.g., via nutrient input), exemplifying how the likelihood of one event is coupled to the likelihood of the other. As for SMHW-SHXs, we know that warm SST anomalies in the nearshore are generally associated with deeper HLDs (S2 Fig; Section 2.6) and that the relatively shallow water columns along the continental shelf are generally well-oxygenated, through a combination of physical (e.g., air-sea interaction, vertical mixing) and biological processes (e.g., photosynthesis; [70]). Coastal hypoxia can result from a sufficiently strong upwelling event that transports cold, low-oxygen, and nutrient-rich waters onto the shelf, a process that is generally more likely to be associated with a marine cold spell (MCS) than a MHW, and a high chlorophyll extreme (HCX) than a LCX (Table 1).

Fig 7. The most common compound extremes over the study period (1996–2019). Maps of the most common compound extreme, defined as the highest number of extreme event days, from a surface (left) and bottom (right) ocean perspective (see respective keys): MHW-LCX (brown), LCX-SHX (purple), MHW-SHX (teal). Light gray contours outline the CCLME, offshore, and nearshore boundaries (see Fig 1 for reference). The maps on the right are regions isolated from the black open squares indicated on the left, delineated by zone 1–4 latitudes; here, only locations found within the CCLME where the ocean bottom is 1000 *m* or shallower are shown.

From a bottom ocean perspective, the continental shelf and slope are most commonly subject to one of two compound extremes, depending on the underlying bathymetry (Fig 7). In general, BMHW-LCXs are most common in relatively shallow water columns, such as along the

This manuscript is a preprint and has not been peer reviewed. The copyright holder has made the manuscript available under a Creative Commons Attribution 4.0 International (CC BY) license and consented to have it forwarded to EarthArXiv for public posting.

continental shelf or island chains, while BMHW-SHXs are most common at locations characterized by relatively deeper water columns along the continental slope. For most of the coastline, this translates to a general cross-shore transition across the shelf break from BMHW-LCXs to BMHW-SHXs as 'most common' from east to west, respectively (Fig 7). This pattern likely reflects differences in hypoxia persistence, where shallower shelf waters typically experience seasonal hypoxia, while deeper slope waters are more likely to be hypoxic for the majority—or entirety—of the year, enabling a more consistent and extensive HLD. The SCB stands out as one exception, characterized by a relatively wide continental shelf with complex topography including multiple islands, with localized and variable patterns of upwelling and stratification. For the majority of the SCB shelf, we find that BMHWs are more likely to co-occur with SHXs (LMF$>$1) and less likely to co-occur with LCXs (LMF$<$1; S5 Fig). Here, BMHWs can be intense and persistent, driven by upwelling dynamics and depth-dependent thermal stratification [32]. Stratified conditions inhibit vertical mixing and oxygen replenishment and can exacerbate hypoxia [38, 71]. While local species experience both BMHW-SHX and BMHW-LCX conditions here, the difference in total days is approximately two months (S4 Fig).

3.3 Spatiotemporal variability in nearshore and offshore ocean properties and their extremes

Seasonal variability of nearshore temperature, $\int$Chl, and HLD (Fig 8e-h) is largely a reflection of the known seasonal variability in physical and biogeochemical processes such as coastal upwelling (e.g., [66]) and organic matter production and respiration [72]. Starting in late spring, surface heating and plentiful light combine with upwelling of cold, nutrient-rich, but oxygen-poor water to drive a productive upper ocean, with shallow HLDs and cold bottom water temperatures (Fig 8e-h). Beginning in late fall, light wanes and upwelling weakens, resulting in a minimally productive surface ocean, more oxygenated water column, and warmer bottom water temperatures (Fig 8e-h). Relative to the nearshore, the offshore region exhibits similar seasonality in SST and $\int$Chl, but is characterized by less phytoplankton biomass and deeper HLDs overall, with seasonal HLD phenology lagging the nearshore by approximately three months (Fig 8 vs. S6 Fig; see discussion in Section 4.2).

Fig 8. Temporal variability of nearshore ocean extremes and their relationship to ENSO phases. Daily time series (1996–2019; solid contours) of (a) SST (red), (b) $\int$Chl (green), (c) HLD (blue; inverted y-axis), and (d) bottom temperature (BT; black) regionally-averaged over the nearshore (0–75 km) coastal band (zones 1–4; see Methods). Additional contours in (a)-(d) show the daily climatology (dotted-dashed) and seasonally-varying percentile threshold (dashed; 90th for temperature, 10th otherwise). Extreme events of each ocean variable are indicated with under-the-curve and vertical shading. The duration of simulated El Niño (brown) and La Niña (teal) phases are indicated along the time (x) axis in (a)-(d), defined when the GLORYS-BGC Niño 3.4 index exceeds ± 1 standard deviation. (e-h) The same climatology shown in (a)-(d) is presented and enlarged as a single annual cycle beginning January 1, respectively.

Interannual variability of temperature, $\int$Chl, and HLD and the timing of their extremes (Fig 8a-d) is largely a reflection of the influence of large-scale modes of climate variability, particularly ENSO, on the CCS thermocline (Figs 8a-d, S6 Fig-S11 Fig; see [64] and references therein). In general, we find that nearshore SMHWs, LCXs, and BMHWs tend to occur during the strong El Niño events of 1997–1998 and 2015–2016, as well as the 2014–2015 Blob period (Figs 8a-b,d, S7 Fig-S8 Fig and S10 Fig; [73]). In contrast, nearshore SHX occurrence is generally associated with La Niña conditions, specifically the strong 2007–2008 and 2010–2011 events (Figs 8c and S9 Fig). However, nearshore HLD appears to exhibit a greater degree of

This manuscript is a preprint and has not been peer reviewed. The copyright holder has made the manuscript available under a Creative Commons Attribution 4.0 International (CC BY) license and consented to have it forwarded to EarthArXiv for public posting.

lower frequency variability compared to temperature and chlorophyll (Figs 8) and S7 Fig-S9 Fig). While decadal modes of variability can modulate ENSO and mediate its influence on the CCS (e.g., [35]), this decadal modulation is less evident in SST and $\int$Chl, instead reflecting higher frequency surface variability (i.e., the forcing that drives these changes is more pronounced on shorter timescales). We also find that the timing of HLD extremes is lagged both in the cross- (Fig 8 vs. S6 Fig) and along-shore direction (S9 Fig), reflective of the low-frequency variability imparted by the large-scale circulation of the region (see discussion in Section 4.2).

During the strong El Niño events of 1997–1998 and 2015–2016, the nearshore is characterized by SMHWs, LCXs, and BMHWs, as well as deep HLDs (Figs 8-9). Indeed, the strongest nearshore deep hypoxia extreme (DHX; Table 1; 3.1σ maximum intensity on March 26, 1998) occurred during the 1997–1998 El Niño, at a time when the region was experiencing surface-to-bottom MHW and 0–100 m LCX conditions (intermediate depths not shown in the former case). In the offshore region, a DHX began approximately 3-4 months after the nearshore one in 1997–1998, while no DHXs were observed during the 2015–2016 event, instead exhibiting shallower-than-normal HLDs, likely explained by low-frequency HLD variability and highlighting event-to-event differences in the CCS response to ENSO (S6 Fig; see [73]). One of the main differences between these two events, both among the strongest on record, lies in their distinct atmospheric drivers and the subsequent impacts on coastal upwelling. In particular, the 1997–1998 event was associated with more severe reductions in upwelling strength than the 2015–2016 event [74].

Fig 9. Annual snapshots of nearshore extremes during five case study periods. Daily time series (solid contours) of nearshore extreme variables (rows; same as in Fig 8) isolated during a single year (July 1–June 30) of five case study periods (columns): from left to right, 1997–1998 (El Niño), 2007–2008 (La Niña), 2010–2011 (La Niña), 2014–2015 ("Blob"), and 2015–2016 (El Niño), respectively. Additional contours indicate the daily climatology (dotted) and both the 90th and 10th percentiles (dashed). High and low extreme events of each ocean variable are indicated with gray under-the-curve and vertical shading (refer to Table 1). Note the inverted y-axis for HLD (third row).

Immediately preceding the strong 2015–2016 El Niño, the onset and peak of the Blob in 2013–2015 occurred against the backdrop of weak or aborted El Niño conditions (not shown), when SST anomalies in the central equatorial Pacific and warm preconditioning along the coast may have aided its impact on the CCS (see [73, 75]). As such, impacts to the nearshore during the Blob period resembled those of a strong El Niño event, including surface and bottom MHWs and LCXs (Figs 8-9), but with relatively weaker and shorter BMHWs and without the DHXs (Fig 9). Indeed, the nearshore experienced only slightly deeper-than-normal HLDs during this period (Figs 8-9), while the offshore saw the end of a long-lasting SHX that began in late 2013, following a period of recurrent La Niña-like conditions since 2005 (S6 Fig).

The La Niña events of 2007–2008 and 2010–2011 are characterized by nearshore SHXs, with a strong and long-lasting SHX during the former and a relatively short and weak SHX during the latter (Fig 9). These La Niña periods are also characterized by HCXs as well as MCSs in both the nearshore (Fig 9) and offshore (S6 Fig), as we would expect from enhanced trade winds and coastal upwelling. On average, the nearshore experienced strong and persistent SHXs during the 2007–2008 La Niña, with conditions lingering well into 2009 (Figs 8c and 9), likely associated with a weaker second-year La Niña in 2008–2009. While the offshore region also saw shallow HLDs during this time, it was not until the end of the 2010–2011 La Niña that HLDs shoaled to an extremely shallow depth, with recurring SHXs through 2014 (S6 Fig). The temporal and regional differences in SHX timing in and around La Niña events likely reflects the diversity of individual events and therefore the diversity in the CCS response to ENSO. In this case, the former was generally classified as a classic Eastern Pacific (EP) La Niña, with the potential for more direct and immediate effects on the west coast thermocline, whereas the latter

This manuscript is a preprint and has not been peer reviewed. The copyright holder has made the manuscript available under a Creative Commons Attribution 4.0 International (CC BY) license and consented to have it forwarded to EarthArXiv for public posting.

event was classified as a Central Pacific (CP) La Niña, and likely to have a more delayed response in the CCS. While both are associated with enhanced coastal upwelling along the west coast, the location of the SST anomalies in the equatorial Pacific–known as ENSO diversity–may play an important role in shaping the associated atmospheric and oceanic teleconnections (see [76]), affecting the likelihood of extreme ocean conditions along the U.S. west coast [77], albeit with a large spread due to internal atmospheric variability [78].

We compare composite anomaly profiles of temperature, chlorophyll, and dissolved oxygen during all identified extreme events across the study period to average anomaly profiles derived from five case study one-year periods (S11 Fig; the same case study periods used in Fig 9). Across zones 1–8, composites represent the typical vertical structure associated with each type of extreme event, while the case study profiles reflect conditions during individual one-year periods characterized by distinct ENSO phases. Composites of extreme events largely reflect the physical and biogeochemical response to the ENSO state, consistent with Turi et [64] (S11 Fig). In general, composite MHW and LCX profiles mirror those during the three warm periods that include the 1997–1998 and 2015–2016 El Niño events and the 2014–2015 Blob. During MHWs, there is a subsurface maximum temperature in the upper 100 *m* and with decreasing magnitude moving northward. During LCXs, the upper 170 *m* is characterized by anomalously low chlorophyll in the near-surface and high chlorophyll in the subsurface, with the inflection point found within the upper 100 *m*. In contrast, composite SHX profiles mirror those during the two cold periods that include the 2007–2008 and 2010–2011 La Niña events. During SHXs, oxygen concentration is slightly elevated at the surface and reduced in the subsurface, a pattern that diminishes northward and offshore, with decreasing resemblance to the cold-period profiles; during La Niña periods, this vertical structure reflects the thermal (solubility) and non-thermal (physical, biological) drivers of oxygen, respectively [64].

3.4 The most widespread extremes in the CCLME

How widespread are any of these extremes at a given time? During the 1997–1998 and 2014–2016 warm periods, SMHWs covered up to 80% and $\sim$100% of the CCLME, respectively (Fig 10a). The same holds true in the offshore band (Fig 10b) while nearshore coverages reached 100% during both periods (Fig 10c), reflecting the regional differences in their climate impacts (see Section 3.3). As such, the most widespread single extreme during this 24 year period is the SMHW, covering 99.2% of the CCLME on March 29, 2015 (Fig 10a).

Fig 10. Spatial extent of single and compound extremes across the CCLME. Time series of the total area affected by single (top panels) and compound (bottom panels) extremes, expressed as a percentage of the (a) CCLME, (b) offshore (making up 34.8% of the CCLME), and (c) nearshore (making up 13.9% of the CCLME). Note, y-axes ranges for compound extremes (bottom panels) differ between regions.

While LCX and SMHW-LCX prevalence is also elevated during El Niño-related warm periods, the first half of 1996 features the most widespread of these extremes, covering up to 55% and 35% of the CCLME, respectively (Fig 10a). This occurs during the tail end of a weak-to-moderate La Niña event in 1995–1996 (not shown). Despite the persistence of cold tropical conditions typically associated with La Niña into 1997, atmospheric circulation in late 1995 sets up anomalously warm SST conditions along the west coast of North America in early 1996 (see [79]), highlighting event-to-event differences in ENSO impacts. These localized warm conditions in early 1996 are not typical of a La Niña pattern, and the most widespread compound extreme, the SMHW-LCX, covers 35.2% of the CCLME on May 16, 1996 (Fig 10a). This underscores the importance of understanding how atmospheric circulation and local dynamics, rather than canonical ENSO states alone, can influence extreme events (see discussion in Section 4.2).

This manuscript is a preprint and has not been peer reviewed. The copyright holder has made the manuscript available under a Creative Commons Attribution 4.0 International (CC BY) license and consented to have it forwarded to EarthArXiv for public posting.

We find that SMHW-SHXs and SMHW-LCX-SHXs are most prevalent outside of the nearshore and during El Niño-related warm periods (Fig 10), a result largely obscured in a regional average (e.g., S6 Fig). At times during the 2014–2016 warm period, SMHW-SHXs cover nearly 15% of both the CCLME and its offshore band, fractional areas on par with SMHW-LCX coverage during that time (Fig 10a-b); the nearshore region appears to be largely unaffected by this particular compound extreme, as well as LCX-SHXs (Fig 10c). As for triple extremes, albeit a relatively rare occurrence, maximum coverage peaks at 1.4% of the CCLME on October 17, 2015 (Fig 10a) and 3.1% for the offshore band on November 15, 2014 (Fig 10b). Indeed, during the Blob, triple extremes covered nearly 15% of zone 7 by the end of 2014 (not shown), the largest fractional area covered by triple extremes at any one time in any of the 8 coastal zones; in zone 7, triple extremes can reach standardized intensities (Ψ') as high as 4.6σ and can last as long as 78 days (Fig 6).

In a regionally-averaged sense, we have so far shown that SHX occurrence is generally associated with strong La Niña conditions, such as during the 2007–2008 and 2010–2011 events. However, retaining the spatial dimension and quantifying the fractional area subjected to SHXs over time provides additional insights (Fig 10). Most notably, the spatial extent of SHXs exhibits relatively greater low frequency variability compared to other extremes, consistently covering between 2% and 23% of the CCLME at any given time over the study period, with maximum coverage occurring in 2012 (22.1%; Fig 10a). While conditions associated with the recurring La Niña period between 2005 and 2012 could have contributed to the 2008 and 2012 peaks in SHX fractional area (Fig 10a-b), the comparable area values that persist after 2012 occur during a generally El Niño-dominated period. We speculate that the low frequency spatiotemporal variability in SHXs identified outside of the nearshore band (Fig 10) is additionally driven by large-scale decadal variability in the region (e.g., gyre-scale circulation; see discussion in Section 4.2). Conversely, the SHX-La Niña relationship is more evident and strongest in the nearshore and exhibits higher frequency variability, with fractional areas peaking during La Niña events, between 20–40% during any of the 1999-2000, 2007–2008, 2010–2011, and 2011-2012 events (Fig 10c).

4 Discussion

4.1 Multi-stressors

Oceanic extreme events can alter both bottom-up (resource-driven) and top-down (predator-driven) ecosystem controls in unique and complex ways. As the landscape of compound extremes continues to shift in a rapidly changing world, the impacts to local food web dynamics and overall community structure become even more complex. While we show that the most common compound extreme in the CCLME is the SMHW-LCX (Fig 7) and that a triple MHW-LCX-SHX compound extreme is a relatively rare occurrence (Figs 4 and 8), scientists and managers would benefit from a future comprehensive analysis of CCLME extremes that further includes combinations of additional known stressors, such as acidity and nutrients.

Like this study, previous research on compound extremes has analyzed combinations of up to three distinct physical and biogeochemical stressors (e.g., [54, 80]). Lack of archived daily output of GLORYS-BGC pH precludes its explicit inclusion in this analysis of extremes, but we can assess the magnitude of its standardized monthly anomalies and comment on the timing of presumed multi-stressors (Fig 11). For example, during the 2007–2008 La Niña event, anomalously low pH values ($<-1.5\sigma$) would suggest that in addition to a nearshore SHX (Fig 9), the ecosystem was additionally subject to acidic conditions, potentially threatening the ability of marine organisms like oysters and crabs to calcify [81]. Indeed, corrosive waters between 2007 and 2008 led to substantial larval mortality in commercial oyster hatcheries in the PNW [14].

During the 1997–1998 El Niño event, anomalously low nutrient concentrations ($<-2\sigma$;

This manuscript is a preprint and has not been peer reviewed. The copyright holder has made the manuscript available under a Creative Commons Attribution 4.0 International (CC BY) license and consented to have it forwarded to EarthArXiv for public posting.

Fig 11. Nearshore physical and biogeochemical variability in relation to ENSO phase. (a) From top to bottom, time series of monthly standardized anomalies of the Niño 3.4 climate index (brown bars) and nearshore-averaged monthly standardized anomalies of SST (red bars), $\int$Chl (green bars), HLD (blue bars), thermocline depth (TD; 3-month running mean; green contour), mixed layer depth (MLD; 3-month running mean; red contour), CUTI (gray bars; black contour indicates the 3-month running mean), vertically-integrated (0–100 m) net primary production ($\int$NPP; green bars), 100 m pH (pink bars), and 100 m nitrate (N; teal bars), phosphate (P; gold bars), and silicate (Si; purple bars) concentrations, respectively. All y-axes values have been restricted to a common range and are expressed in sigma units. (b-c) Schematic representation of a simplified view of some of the locally- and remotely-forced responses expected in the nearshore CCLME during a (b) El Niño and (c) La Niña. Positive (+) and negative (−) anomalies in atmospheric winds (northerly, out of the page; southerly, into the page), sea level pressure (SLP), the strength of the Aleutian Low (AL), the type of coastally trapped waves (CTWs; upwelling (↑) or downwelling (↓)), sea surface height (SSH), abundance of primary producers (star and oval shapes), temperature, TD (dashed line), upwelling (solid arrow), pH, oxygen concentration, and nutrient concentration (vertical colored gradient, where darker indicates higher). For illustrative purposes, size, weight, or density is used to indicate the relative differences in scalar properties between ENSO phases.

Fig 11a) are likely drivers of LCX conditions (Fig 9), while high pH values ($>2\sigma$) indicate a reprieve from ocean acidification (Fig 11a). While low nutrient availability can lead to LCXs, it can also contribute to HCXs under specific conditions. Some HCXs can be classified as harmful algal blooms (HABs) when certain toxin-producing phytoplankton (e.g., *Pseudo-nitzschia*) dominate, though such complex biogeochemical dynamics are not simulated in GLORYS-BGC. A striking example occurred in 2015, when an extensive and toxic *Pseudo-nitzschia*-based HAB poisoned food webs and closed fisheries along the U.S. west coast [10]. Ryan et al. [82] showed that this diatom bloom followed a strong upwelling event that injected nutrients into coastal waters, though with an anomalously low silicate-to-nitrate (Si:N) ratio signature. These silicate-limited, nitrate-replete conditions supported dense diatom populations and may have promoted elevated toxin production (see [82] and references therein). Consistent with observed conditions, GLORYS-BGC captures persistently low Si:N ratios beginning during the Blob and extending through the 2015–2016 El Niño (Fig 11a), reaching a 24-year nearshore minimum (-0.25) on March 16, 2016 (not shown). Laboratory and field studies have shown that *Pseudo-nitzschia* from the CCS can thrive under warm anomalies and low Si extremes (Si limitation) and produce higher amounts of toxin, particularly when also exposed to acidic conditions [83]. Improving our understanding of the drivers and interactions of nutrient extremes–not just their absolute concentrations but also their stoichiometric ratios–is critical for advancing multi-stressor research, predictive capabilities, and risk management.

Our results and their limitations highlight the need for creating and maintaining observational platforms capable of capturing concurrent extremes. Satellites provide the greatest spatiotemporal resolution in the study of oceanic extremes, but are currently limited to surface ocean color- and SST-based events. For example, satellite chlorophyll retrievals are proxies for the total amount of phytoplankton present, with no distinguishing information on community structure. While some studies have attempted to infer phytoplankton functional types using post-hoc algorithms applied to standard ocean color products, these methods have generally been considered experimental, with limited accuracy and reliability. In contrast, NASA's recently launched Plankton, Aerosol, Cloud, ocean Ecosystem (PACE) mission integrates advanced algorithms for phytoplankton group discrimination directly into its standard data processing, representing a significant step forward for future observational studies of LCXs and HABs. In situ observations (e.g., moorings, floats, gliders, ships) suffer from lower spatiotemporal resolution and/or coverage, but often boast a suite of concurrent measurements, including temperature, chlorophyll, oxygen, nutrients, and/or pH from which to study many

This manuscript is a preprint and has not been peer reviewed. The copyright holder has made the manuscript available under a Creative Commons Attribution 4.0 International (CC BY) license and consented to have it forwarded to EarthArXiv for public posting.

multi-stressors. Global and regional ocean reanalyses marry model output with observations to produce gap-free products, and the relatively few that include biogeochemistry are critical to the continued study of multi-stressors.

4.2 Characterizing compound extreme events to inform marine resource management

We show that MHWs, LCXs, SHXs, and their combinations tend to occur during strong ENSO periods (Figs 8-10, S6 Fig-S10 Fig). The most common compound extremes in the CCLME are SMHW-LCXs in the nearshore and BMHW-SHXs and BMHW-LCXs along the continental slope and shelf, respectively (Fig 7). The ability to skillfully predict such extremes on subannual-to-decadal timescales would support coastal management (e.g., see [84]), such as the near-term decision to proactively close a fishery ahead of a strong MHW in an attempt to mitigate impacts. Seasonal-to-interannual forecasts leveraging ENSO as a source of predictability have already demonstrated skill for MHWs, ocean acidification extremes, and even chlorophyll anomalies in the CCS (e.g., [7, 85–87]).

Taking a generalized view of large-scale climate variability on interannual-to-decadal timescales, we interpret standardized monthly anomalies in ecosystem-relevant quantities (Fig 11a) and present a schematic of a simplified view of the ENSO-CCLME relationship from 1996–2019 (Fig 11b-c). During the strong El Niño events of 1997–1998 and 2015–2016 (Fig 11a-b), the nearshore ocean was characterized by elevated sea surface height (SSH), deeper thermocline and mixed layer depths, weaker upwelling (quantified by the coastal upwelling transport index, or CUTI; [66]), warmer SST, deeper HLD, higher pH (i.e., more basic conditions), and lower concentration of the macronutrients nitrate, phosphate, and silicate at 100 m (below the thermocline), along with reduced bulk chlorophyll and net primary production (Fig 11a). In contrast, during the strong La Niña events of 2007–2008 and 2010–2011, the opposite patterns generally occurred (Fig 11a,c); however, the response in monthly thermocline and mixed layer depths during La Niña is less consistent and more dependent on coastal location (see [88]). These relationships align with previous modeling studies that highlight event-to-event variability in ENSO impacts along the coast (e.g., [64, 73].

While ENSO may have predictive power, it is important to remember that there is still uncertainty associated with the CCLME response to ENSO and more research on quantifying this uncertainty is needed. Drawing on an example from Section 3.4, in the seasons following the moderate 1995–1996 La Niña (not shown), our results show SMHWs and SMHW-LCXs extending unusually far across the CCLME–at areal extents more typically seen during weak-to-moderate El Niño conditions (e.g., up to $\sim$15% in 2018-2019; Fig 10b-c). This occurred despite continued tropical La Niña conditions into 1996–1997, likely due to an atmospheric circulation setup over the Northeast Pacific that favored warm SST conditions in early 1996 (not shown; see [79]). Such examples from our analysis underscore the importance of exercising caution when attributing local extremes solely to canonical ENSO phases.

Decadal variability may also provide a potential source of predictability. We know that the combined effects of physical (e.g., circulation) and biological (e.g., respiration) variability set the low-frequency variability of oxygen in the thermocline [89]. For the CCS, gyre-scale circulation of the North Pacific plays an important role in modulating subsurface oxygen through the propagation of water mass anomalies on decadal timescales [90, 91]. For example, subsurface advection injects relatively young water masses with a high oxygen signature from the North Pacific gyre into the CCS ([90] and references therein). The predictability of oxygen and other ocean tracers (e.g., [92]) derives from the multiyear memory associated with these gyre-scale drivers [91]. The California Undercurrent has additionally been cited as an important source of water mass anomalies in the nearshore CCS, transporting relatively old water masses with little-to-no oxygen from the tropics northward along its path [93]. One additional hypothesis suggests that the PDO and/or NPGO generate this low-frequency variability, yet,

This manuscript is a preprint and has not been peer reviewed. The copyright holder has made the manuscript available under a Creative Commons Attribution 4.0 International (CC BY) license and consented to have it forwarded to EarthArXiv for public posting.

similar to the findings of Pozo Buil and Di Lorenzo [91], we find statistically non-significant correlations between HLD and the PDO or NPGO indices (not shown). Recognizing that the PDO and NPGO are indices of statistical modes of variability that represent the summarized effects of underlying physical processes, we underscore the need to focus on these component physical processes, which may play a more direct role in modulating oxygen variability and extremes in the CCS. For example, the PDO reflects shifts in wind patterns, ocean circulation, and the advection of water masses, all of which influence oxygen levels and may be critical drivers of extremes [34]. More research is needed to better reconcile the potential interaction between gyre-scale and undercurrent drivers in (1) modulating nearshore HLD variability and extremes on seasonal-to-decadal timescales, (2) lending predictive skill, and (3) playing a role, if any, in the apparent lag we observe in the seasonality of HLD and timing of extremes in the along-shore and off-shore directions. Despite these complexities, to first order, water column dissolved oxygen–and thus, HLD variability–is not fully understood, attributable to a historical lack of long-term, sustained observations across broad spatial scales on these timescales.

5 Conclusions

The abrupt and oftentimes compounding nature of extreme events could test the resilience of marine ecosystems, as those players unable to acclimate in time could contribute to a major restructuring of the community, with ecological, social, and economic consequences. For the CCLME, we have demonstrated that extremes in temperature, upper ocean chlorophyll concentration, and hypoxic layer depth impact vertical habitable space and show that their frequency, intensity, and duration varies by region and state of ENSO. Of these, marine heatwave-low chlorophyll extremes have been the most common compound extreme observed within 75 km of the coastline since 1996. This study also describes how large-scale climate variability and low-frequency variability can play a role in modulating these properties on seasonal-to-decadal timescales and the timing of their extremes, while potentially providing sources of predictability that can be leveraged in future studies. Research into the predictability of single oceanic extremes is active and ongoing, but still in its infancy. Indeed, our ability to predict compound extremes has largely not been assessed. For now, managers, fishers, and stakeholders can benefit from this ecosystem-wide characterization of these physical and biogeochemical extremes and their spatiotemporal hotspots.

Supporting information

S1 Fig. (a-b) Time series of daily CCLME-averaged SST (solid contour) and 90th percentile (dotted) from (b) GLORYS-BGC (black) and (c) OISSTv2 (red) from 1996 to 2019. Surface MHWs (SMHWs) in (a) and (b) are indicated by under-the-curve and vertical gray shading; any simulated SMHWs that were not also observed ('missed') are indicated by red vertical shading in (a). The POD of SMHWs identified from CCLME-average SSTs is 82%. (c) Probability (%; color) of SMHW detection (POD) at each GLORYS-BGC grid point within the CCLME over the study period.

S2 Fig. Scatter plots of observed (red) and simulated (black) seasonal standardized anomalies (filled circles) of SST and HLD (top row), SST and 0–100 m integrated chlorophyll concentration ($\int$CHL; middle row), and HLD and $\int$CHL (bottom row) from stations along 6 CalCOFI lines (map inset; stations overlain on grayscale bathymetry from GLORYS-BGC). Also shown are regression lines with corresponding regression coefficients, r, and 95% confidence ellipses. Properties were first averaged over the nearshore (0–75 km from the coast; gold circles on map; right column of scatter plots) and offshore (75–300 km; teal circles on map;

This manuscript is a preprint and has not been peer reviewed. The copyright holder has made the manuscript available under a Creative Commons Attribution 4.0 International (CC BY) license and consented to have it forwarded to EarthArXiv for public posting.

left column of scatter plots) coastal bands of the CCLME. Also shown with scatter plots are regression lines with corresponding regression coefficients, r, and 95% confidence ellipses.

S3 Fig. Scatter plots of observed (x-axis) and simulated (y-axis) seasonal standardized anomalies (open black circles) of SST (top row), 0–100 m integrated chlorophyll concentration ($\int$Chl; middle row), and HLD (bottom row) from stations along 6 CalCOFI lines, first averaged over the offshore (75-300 km; left column) and nearshore (0-75 km from the coast; right column) coastal bands of the CCLME (see map inset in S2 Fig). Five case study years (July 1–June 30) are indicated by distinct markers and colored by the general ENSO phase (magenta = warm, teal = cool; see key). The 1:1 line is shown in black and correlation coefficients (r) are annotated.

S4 Fig. Maps of the number of compound extreme days (color; minimum of five days, by definition) identified over the study period (1996–2019) from a surface (first row) and bottom (second row) ocean perspective: (columns) from left to right, MHW-LCX, LCX-SHX, MHW-SHX, and MHW-LCX-SHX, respectively. Light gray contours outline the CCLME, offshore, and nearshore boundaries (see Fig 1 for reference). (second row) Only locations found within the CCLME (black contour) where the ocean bottom is 1000 m or shallower are shown.

S5 Fig. The likelihood multiplication factor (LMF; color) for each compound extreme (columns) from a surface (first row) and bottom (second row) ocean perspective: (columns) from left to right, MHW-LCX, LCX-SHX, MHW-SHX, and MHW-LCX-SHX, respectively. By definition, an LMF = 1 indicates the two or more extremes are statistically independent. For a given compound extreme, the absence of color (white) indicates no event has been identified over the study period (LMF = 0). (second row) Only locations found within the CCLME (black contour) where the ocean bottom is 1000 m or shallower are shown.

S6 Fig. As in Fig 8, but for the offshore (75–300 km) coastal band (zones 5–8) and without bottom temperature.

S7 Fig. (left panels) Daily time series (1996–2019; solid contours) of SST (red) from north (top; zone 4) to south (bottom; zone 1) in the nearshore. Additional contours show the daily climatology (dotted-dashed) and seasonally-varying percentile threshold (90th; dashed). Extreme events are indicated with under-the-curve and vertical shading. The duration of simulated El Niño (brown) and La Niña (teal) phases are indicated along the time (x) axis, defined when the Niño3.4 index exceeds ± 1 standard deviation. (right panels) The daily climatology for each zone is presented and enlarged as a single annual cycle beginning January 1 (dotted-dashed).

S8 Fig. As in S7 Fig, but for $\int$Chl (green solid contour) and its 10th percentile (dashed).

S9 Fig. As in S7 Fig, but for HLD (blue solid contour) and its 10th percentile (dashed). Note the inverted y-axes.

S10 Fig. As in S7 Fig, but for bottom temperature (black solid contour) and its 90th percentile (dashed).

S11 Fig. Composite average anomaly profiles (black dashed contour) of upper ocean temperature (left), chlorophyll (middle), and oxygen (right) during extreme events relative to the full study period (1996–2019). Annual anomaly profiles (solid contours) of each case study period (July 1–June 30) relative to the full study period: 1997–1998 (yellow), 2007–2008 (green), 2010–2011 (blue), 2014–2015 (red), and 2015–2016 (purple). For each variable, the

This manuscript is a preprint and has not been peer reviewed. The copyright holder has made the manuscript available under a Creative Commons Attribution 4.0 International (CC BY) license and consented to have it forwarded to EarthArXiv for public posting.

nearshore zones 1–4 are displayed on the right and offshore zones 5–8 on the left, just as they appear in Fig 1 (zone numbers increase from south to north). Note, depth ranges (y-axes) differ between variables.

Acknowledgments

We appreciate the time spent discussing vertically-migrating species in this region with Kelly Benoit-Bird (MBARI) and ecosystem dynamics with Kristen Krumhardt (NCAR). We acknowledge the invaluable contributions made through the CalCOFI program year after year by both science and crew. This research was supported in part by the NOAA cooperative agreement NA22OAR4320151, for the Cooperative Institute for Earth System Research and Data Science (CIESRDS). Antonietta Capotondi was supported by the NOAA Climate Program Office under CVP Award NA24OARX431C0021.

Data Availability Statement

All data and code used to produce the figures in this study are archived in the following Zenodo repository: https://doi.org/10.5281/zenodo.15313482. The FREEBIORYS2V4 ocean biogeochemistry hindcast output is available from the Copernicus Marine Environment Monitoring Service (CMEMS; https://doi.org/10.48670/moi-00019); the physical variables from the FREEGLORYS2V4 ocean hindcast were made available upon request. Satellite-derived ESA-CCI chlorophyll concentrations are available at http://www.esa-oceancolour-cci.org/. NOAA OISSTv2.1 high-resolution sea surface temperatures were provided by the NOAA Physical Sciences Laboratory and can be accessed at https://psl.noaa.gov/data/gridded/data.noaa.oisst.v2.highres.html. CalCOFI data is publicly available at https://calcofi.org/. CUTI indices derived from the University of California Santa Cruz (UCSC) regional ocean reanalysis (https://oceanmodeling.ucsc.edu/) are continuously updated and made available at https://oceanview.pfeg.noaa.gov/products/upwelling/.

Author Contributions

Conceptualization: Natalie M. Freeman, Gaëlle Hervieux, Michael A. Alexander, Michael G. Jacox, Dillon J. Amaya, James D. Scott
Data curation: Gaëlle Hervieux, Dillon J. Amaya
Formal analysis: Gaëlle Hervieux
Investigation: Gaëlle Hervieux
Methodology: Natalie M. Freeman, Gaëlle Hervieux, Michael A. Alexander, Michael G. Jacox, Dillon J. Amaya, James D. Scott
Project administration: Natalie M. Freeman, Gaëlle Hervieux, Michael A. Alexander
Software: Gaëlle Hervieux
Supervision: Natalie M. Freeman, Gaëlle Hervieux, Michael A. Alexander, Antonietta Capotondi
Validation: Natalie M. Freeman, Gaëlle Hervieux, Michael A. Alexander, Michael G. Jacox, Dillon J. Amaya, James D. Scott
Visualization: Natalie M. Freeman, Gaëlle Hervieux, Michael A. Alexander, Michael G. Jacox, Dillon J. Amaya, James D. Scott
Writing – original draft: Natalie M. Freeman
Writing – reviewing & editing: Natalie M. Freeman, Gaëlle Hervieux, Michael A. Alexander, Michael G. Jacox, Dillon J. Amaya, James D. Scott, Antonietta Capotondi

This manuscript is a preprint and has not been peer reviewed. The copyright holder has made the manuscript available under a Creative Commons Attribution 4.0 International (CC BY) license and consented to have it forwarded to EarthArXiv for public posting.

References

1. Chavez FP, Messié M. A comparison of Eastern Boundary Upwelling Ecosystems. Progress in Oceanography. 2009; 83.
2. Capotondi A, Rodrigues RR, Gupta AS, Benthuysen JA, Deser C, Frölicher TL, et al. A global overview of marine heatwaves in a changing climate. Communications Earth & Environment. 2024; 5(1).
3. Bond NA, Cronin MF, Freeland H, Mantua N. Causes and impacts of the 2014 warm anomaly in the NE Pacific. Geophysical Research Letters. 2015; 42(9).
4. Amaya DJ, Miller AJ, Xie SP, Kosaka Y. Physical drivers of the summer 2019 North Pacific marine heatwave. Nature Communications. 2020; 11(1):1903.
5. Capotondi A, Newman M, Xu T, Di Lorenzo E. An optimal precursor of northeast pacific marine heatwaves and central pacific El Niño events. Geophysical Research Letters. 2022; 49(5).
6. Jacox MG, Tommasi D, Alexander MA, Hervieux G, Stock CA. Predicting the evolution of the 2014–2016 California current system marine heatwave from an ensemble of coupled global climate forecasts. Frontiers in Marine Science. 2019; 6.
7. Jacox MG, Alexander MA, Amaya D, Becker E, Bograd SJ, Brodie S, et al. Global seasonal forecasts of marine heatwaves. Nature. 2022; 604:486–490.
8. Smale DA, Wernberg T, Oliver ECJ, Thomsen M, Harvey BP, Straub SC, et al. Marine heatwaves threaten global biodiversity and the provision of ecosystem services. Nature Climate Change. 2019; 9(4):306–312.
9. Cavole L, Demko AM, Diner R, Giddings A, Koester I, Pagniello C, et al. Biological impacts of the 2013–2015 warm-water anomaly in the northeast pacific: Winners, losers, and the future. Oceanography. 2016; 29(2).
10. McCabe RM, Hickey BM, Kudela RM, Lefebvre KA, Adams NG, Bill BD, et al. An unprecedented coastwide toxic algal bloom linked to anomalous ocean conditions. Geophysical Research Letters. 2016; 43(19):10366–10376.
11. Hamilton SL, Kennedy EG, Zulian M, Hill TM, Gaylord B, Sanford E, et al. Variable exposure to multiple climate stressors across the California marine protected area network and policy implications. ICES Journal of Marine Science. 2023; 80(7):1923–1935.
12. Friedland KD, Stock C, Drinkwater KF, Link JS, Leaf RT, Shank BV, et al. Pathways between primary production and fisheries yields of large marine ecosystems. PloS One. 2012; 7(1).
13. Grantham BA, Chan F, Nielsen KJ, Fox DS, Barth JA, Huyer A, et al. Upwelling-driven nearshore hypoxia signals ecosystem and oceanographic changes in the northeast Pacific. Nature. 2004; 429(6993):749–754.
14. Barton A, Hatchery WCS, Waldbusser G, Feely R, Weisberg S, Newton J, et al. Impacts of coastal acidification on the pacific northwest shellfish industry and adaptation strategies implemented in response. Oceanography. 2015; 25(2):146–159.
15. Singh D, Crimmins AR, Pflug JM, Barnard PL, Helgeson JF, Hoell A, et al. Focus on Compound Events. In: Crimmins AR, Avery CW, Easterling DR, Kunkel KE, Stewart BC, Maycock TK, editors. Fifth National Climate Assessment. Washington, DC, USA: U.S. Global Change Research Program; 2023.

This manuscript is a preprint and has not been peer reviewed. The copyright holder has made the manuscript available under a Creative Commons Attribution 4.0 International (CC BY) license and consented to have it forwarded to EarthArXiv for public posting.

16. Barbeaux SJ, Holsman K, Zador S. Marine heatwave stress test of ecosystem-based fisheries management in the gulf of Alaska pacific cod fishery. Frontiers in Marine Science. 2020; 7.

17. Szuwalski CS, Aydin K, Fedewa EJ, Garber-Yonts B, Litzow MA. The collapse of eastern Bering Sea snow crab. Science. 2023; 382(6668):306–310.

18. Lucey N, Aube C, Herwig A, Collin R. Compound extreme events induce rapid mortality in a tropical sea urchin. The Biological Bulletin. 2022; 243(2):239–254.

19. Murie KA, Bourdeau PE. Energetic context determines the effects of multiple upwelling-associated stressors on sea urchin performance. Scientific Reports. 2021; 11:11313.

20. Jorda G, Marbà N, Bennett S, Santana-Garcon J, Agusti S, Duarte CM. Ocean warming compresses the three-dimensional habitat of marine life. Nature Ecology & Evolution. 2020; 4(1):109–114.

21. Jacox MG, Alexander MA, Bograd SJ, Scott JD. Thermal displacement by marine heatwaves. Nature. 2020; 584(7819):82–86.

22. Froehlich HE, Essington TE, Beaudreau AH, Levin PS. Movement Patterns and Distributional Shifts of Dungeness Crab (Metacarcinus magister) and English Sole (Parophrys vetulus) During Seasonal Hypoxia. Estuaries and Coasts. 2014; 37(2):449–460.

23. Briscoe DK, Hobday AJ, Carlisle A, Scales K, Eveson JP, Arrizabalaga H, et al. Ecological bridges and barriers in pelagic ecosystems. Deep-Sea Research Part II. 2017; 140:182–192.

24. Iglesias IS, Fiechter J, Santora JA, Field JC. Vertical distribution of mesopelagic fishes deepens during marine heatwave in the California Current. ICES Journal of Marine Science. 2024; 81(9):1837–1849.

25. Jacox MG, Fiechter J, Moore AM, Edwards CA. ENSO and the California Current coastal upwelling response. Journal of Geophysical Research: Oceans. 2015; 120(3):1691–1702.

26. Benoit-Bird KJ, Battaile BC, Heppell SA, Hoover B, Irons D, Jones N, et al. Prey patch patterns predict habitat use by top marine predators with diverse foraging strategies. PloS One. 2013; 8(1).

27. Bednaršek N, Ohman MD. Changes in pteropod distributions and shell dissolution across a frontal system in the California Current System. Marine Ecology Progress Series. 2015; 523:93–103.

28. Alexander MA, Bladé I, Newman M, Lanzante JR, Lau NC, Scott JD. The atmospheric bridge: The influence of ENSO teleconnections on air–sea interaction over the global oceans. Journal of Climate. 2002; 15(16):2205–2231.

29. Liu Z, Alexander M. Atmospheric bridge, oceanic tunnel, and global climatic teleconnections. Reviews of Geophysics. 2007; 45(2).

30. Frischknecht M, Münnich M, Gruber N. Remote versus local influence of ENSO on the California Current System. Journal of Geophysical Research: Oceans. 2015; 120(2):1353–1374.

This manuscript is a preprint and has not been peer reviewed. The copyright holder has made the manuscript available under a Creative Commons Attribution 4.0 International (CC BY) license and consented to have it forwarded to EarthArXiv for public posting.

31. Amaya DJ, Jacox MG, Dias J, Alexander MA, Karnauskas KB, Scott JD, et al. Subseasonal-to-seasonal forecast skill in the California current system and its connection to coastal Kelvin waves. Journal of Geophysical Research: Oceans. 2022; 127(1).

32. Amaya DJ, Jacox MG, Alexander MA, Scott JD, Deser C, Capotondi A, et al. Bottom marine heatwaves along the continental shelves of North America. Nature Communications. 2023; 14(1):1038.

33. Mantua NJ, Hare SR. The Pacific Decadal Oscillation. Journal of Oceanography. 2002; 58(1):35–44.

34. Newman M, Alexander MA, Ault TR, Cobb KM, Deser C, Di Lorenzo E, et al. The Pacific decadal oscillation, revisited. Journal of Climate. 2016; 29(12):4399–4427.

35. Di Lorenzo E, N S, Cobb KM, Chhak K, S FPJ, Miller AJ, et al. North Pacific Gyre Oscillation links ocean climate and ecosystem change. Geophysical Research Letters. 2008; 35(8).

36. Di Lorenzo E, Combes V, Keister J, Strub PT, Thomas A, Franks P, et al. Synthesis of pacific ocean climate and ecosystem dynamics. Oceanography. 2013; 26(4):68–81.

37. Levitus S, Antonov JI, Boyer TP, Locarnini RA, Garcia HE, Mishonov AV. Global ocean heat content 1955–2008 in light of recently revealed instrumentation problems. Geophysical Research Letters. 2009; 36(7).

38. Bograd SJ, Castro CG, Di Lorenzo E, Palacios DM, Bailey H, Gilly W, et al. Oxygen declines and the shoaling of the hypoxic boundary in the California Current. Geophysical Research Letters. 2008; 35(12).

39. Schmidtko S, Stramma L, Visbeck M. Decline in global oceanic oxygen content during the past five decades. Nature. 2017; 542(7641):335–339.

40. Feely R, Doney S, Cooley S. Ocean acidification: Present conditions and future changes in a high-CO2 world. Oceanography. 2009; 22(4):36–47.

41. Aumont O, Ethé C, Tagliabue A, Bopp L, Gehlen M. PISCES-v2: An ocean biogeochemical model for carbon and ecosystem studies. Geoscientific Model Development. 2015;8(8):2465–2513. doi:10.5194/gmd-8-2465-2015.

42. Garcia HE, Locarnini RA, Boyer TP, Antonov JI, Baranova OK, Zweng MM, et al. World Ocean Atlas 2013, Volume 3: Dissolved Oxygen, Apparent Oxygen Utilization, and Oxygen Saturation. S Levitus, Ed, A Mishonov Technical Ed; NOAA Atlas NESDIS 75. 2013; 27.

43. Dee DP, Uppala SM, Simmons AJ, Berrisford P, Poli P, Kobayashi S, et al. The ERA-Interim reanalysis: configuration and performance of the data assimilation system. Quarterly Journal of the Royal Meteorological Society. 2011; 137(656):553–597.

44. Perruche C, Szczypta C, Paul J, Drévillon M. Global production centre GLOBAL_REANALYSIS_BIO_001_029. Copernicus Marine Environment Monitoring Service. 2019;doi:10.48670/moi-00019.

45. Reijnders D, Bakker DCE, van Sebille E. Disentangling carbon concentration changes along pathways of north Atlantic subtropical mode water. Journal of Geophysical Research: Oceans. 2024; 129(7).

46. Perruche C. Product user manual for the global ocean biogeochemistry hindcast GLOBAL_REANALYSIS_BIO_001_029. Version 1. Copernicus Marine Environment Monitoring Service. 2018;doi:10.25607/OBP-490.

This manuscript is a preprint and has not been peer reviewed. The copyright holder has made the manuscript available under a Creative Commons Attribution 4.0 International (CC BY) license and consented to have it forwarded to EarthArXiv for public posting.

47. Le Grix N, Zscheischler J, Laufkötter C, Rousseaux CS, Frölicher TL. Compound high-temperature and low-chlorophyll extremes in the ocean over the satellite period. Biogeosciences. 2021; 18(6):2119–2137.

48. Hobday AJ, Alexander LV, Perkins SE, Smale DA, Straub SC, Oliver ECJ, et al. A hierarchical approach to defining marine heatwaves. Progress in Oceanography. 2016; 141:227–238.

49. Oliver ECJ, Donat MG, Burrows MT, Moore PJ, Smale DA, Alexander LV, et al. Longer and more frequent marine heatwaves over the past century. Nature Communications. 2018; 9(1):1324. doi:10.1038/s41467-018-03732-9.

50. Köhn EE, Münnich M, Vogt M, Desmet F, Gruber N. Strong habitat compression by extreme shoaling events of hypoxic waters in the Eastern Pacific. Journal of Geophysical Research: Oceans. 2022; 127(6).

51. Vaquer-Sunyer R, Duarte CM. Thresholds of hypoxia for marine biodiversity. Proceedings of the National Academy of Sciences of the United States of America. 2008; 105(40):15452–15457.

52. Li D, Chen Y, Qi J, Zhu Y, Lu C, B, et al. Attribution of the July 2021 record-breaking northwest Pacific marine heatwave to global warming, atmospheric circulation, and ENSO. Bulletin of the American Meteorological Society. 2023; 104.

53. Chen Q, Li D, Feng J, Zhao L, Qi J, Yin B. Understanding the compound marine heatwave and low-chlorophyll extremes in the western Pacific Ocean. Frontiers in Marine Science. 2023; 10.

54. Wong J, Münnich M, Gruber N. Column-compound extremes in the global ocean. AGU Advances. 2024; 5(3).

55. Huang B, Liu C, Banzon V, Freeman E, Graham G, Hankins B, et al. Improvements of the Daily Optimum Interpolation Sea Surface Temperature (DOISST) version 2.1. Journal of Climate. 2021; 34(8):2923–2939.

56. Reynolds RW, Smith TM, Liu C, Chelton DB, Casey KS, Schlax MG. Daily high-resolution-blended analyses for sea surface temperature. Journal of Climate. 2007; 20(22):5473–5496.

57. Sathyendranath S, Brewin RJW, Brockmann C, Brotas V, Calton B, Chuprin A, et al. An ocean-colour time series for use in climate studies: The experience of the ocean-colour climate change initiative (OC-CCI). Sensors. 2019; 19(19):4285.

58. Silva ENS, Anderson BT. Northeast Pacific marine heatwaves linked to Kuroshio Extension variability. Communications Earth & Environment. 2023; 4(1).

59. Atkins J, Andrews O, Frenger I. Quantifying the contribution of ocean mesoscale eddies to low oxygen extreme events. Geophysical Research Letters. 2022; 49(15).

60. Mogollón R. ENSO-driven CO2 efflux variability and the role of the upwelling region on the carbon exchange in the Northern Humboldt Current System. Journal of Marine Systems. 2020; 201(103240):103240.

61. Lefèvre N, Tyaquiçã P, Veleda D, Perruche C, van Gennip SJ. Amazon River propagation evidenced by a CO2 decrease at 8°N, 38°W in September 2013. Journal of Marine Systems. 2020; 211(103419):103419.

This manuscript is a preprint and has not been peer reviewed. The copyright holder has made the manuscript available under a Creative Commons Attribution 4.0 International (CC BY) license and consented to have it forwarded to EarthArXiv for public posting.

62. Lombard F, Bourdin G, Pesant S, Agostini S, Baudena A, Boissin E, et al. Open science resources from the Tara Pacific expedition across coral reef and surface ocean ecosystems. Scientific Data. 2023; 10(1):324.

63. Holzer M. The fate of oxygen in the ocean and its sensitivity to local changes in biological production. Journal of Geophysical Research: Oceans. 2022; 127(8).

64. Turi G, Alexander M, Lovenduski NS, Capotondi A, Scott J, Stock C, et al. Response of O2 and pH to ENSO in the California Current System in a high-resolution global climate model. Ocean Science. 2018; 14(1):69–86.

65. Mantua NJ, Hare SR, Zhang Y, Wallace JM, Francis RC. A pacific interdecadal climate oscillation with impacts on salmon production. Bulletin of the American Meteorological Society. 1997; 78(6):1069–1079.

66. Jacox MG, Edwards CA, Hazen EL, Bograd SJ. Coastal upwelling revisited: Ekman, Bakun, and improved upwelling indices for the U.S. west coast Journal of Geophysical Research: Oceans. 2018; 123(10).

67. de Boyer Montégut C, Madec G, Fischer AS, Lazar A, Iudicone D. Mixed layer depth over the global ocean: An examination of profile data and a profile-based climatology. Journal of Geophysical Research: Oceans. 2004; 109.

68. Zscheischler J, Seneviratne SI. Dependence of drivers affects risks associated with compound events. Science Advances. 2017; 3(6):1–11.

69. Damien P, Bianchi D, Kessouri F, McWilliams JC. Extremes and short-term fluctuations in coastal ocean acidification and hypoxia. Journal of Geophysical Research: Oceans. 2024; 129(11).

70. Helly JJ, Levin LA. Global distribution of naturally occurring marine hypoxia on continental margins. Deep-Sea Research Part I: Oceanographic Research Papers. 2004; 51(9):1159–1168.

71. Booth JAT, Woodson CB, Sutula M, Micheli F, Weisberg SB, Bograd SJ, et al. Patterns and potential drivers of declining oxygen content along the southern California coast. Limnology and Oceanography. 2014; 59(4):1127–1138.

72. Connolly TP, Hickey BM, Geier SL, Cochlan WP. Processes influencing seasonal hypoxia in the northern California Current System. Journal of Geophysical Research: Oceans. 2010; 115.

73. Capotondi A, Sardeshmukh PD, Di Lorenzo E, Subramanian AC, Miller AJ. Predictability of US West Coast Ocean Temperatures is not solely due to ENSO. Scientific Reports. 2019; 9(1):10993.

74. Jacox MG, Hazen EL, Zaba KD, Rudnick DL, Edwards CA, Moore AM, et al. Impacts of the 2015–2016 El Niño on the California Current System: Early assessment and comparison to past events. Geophysical Research Letters. 2016; 43(13):7072–7080.

75. Kurapov AL, Rudnick DL, Cervantes BT, Risien CM. Slope and shelf flow anomalies off Oregon influenced by the El Niño remote oceanic mechanism in 2014–2016. Journal of Geophysical Research: Oceans. 2022; 127(11).

76. Capotondi A, Wittenberg AT, Kug JS, Takahashi K, McPhaden MJ. ENSO Diversity. In: Geophysical Monograph Series. Wiley; 2020. p. 65–86.

This manuscript is a preprint and has not been peer reviewed. The copyright holder has made the manuscript available under a Creative Commons Attribution 4.0 International (CC BY) license and consented to have it forwarded to EarthArXiv for public posting.

77. Gregory CH, Artana C, Lama S, León-FonFay D, Sala J, Xiao F, et al. Global marine heatwaves under different flavors of ENSO. Geophysical Research Letters. 2024; 51(20).

78. Deser C, Simpson IR, McKinnon KA, Phillips AS. The Northern Hemisphere extratropical atmospheric circulation response to ENSO: How well do we know it and how do we evaluate models accordingly? Journal of Climate. 2017; 30(13):5059–5082.

79. Hayward TL, Cummings SL, Cayan DR, Chavez FP, Lynn RJ, Mantyla AW, et al. The state of the California Current in 1995–1996: Continuing declines in macrozooplankton biomass during a period of nearly normal circulation. CalCOFI Reports. 1996;37:22–37.

80. Gruber N, Boyd PW, Frölicher TL, Vogt M. Biogeochemical extremes and compound events in the ocean. Nature. 2021; 600(7889):395–407.

81. Fabry VJ, Seibel BA, Feely RA, Orr JC. Impacts of ocean acidification on marine fauna and ecosystem processes. ICES Journal of Marine Science. 2008; 65(3):414–432.

82. Ryan JP, Kudela RM, Birch JM, Blum M, Bowers HA, Chavez FP, et al. Causality of an extreme harmful algal bloom in Monterey Bay, California, during the 2014–2016 northeast Pacific warm anomaly. Geophysical Research Letters. 2017; 44(11):5571–5579.

83. Tatters AO, Fu FX, Hutchins DA. High CO2 and silicate limitation synergistically increase the toxicity of Pseudo-nitzschia fraudulenta. PloS One. 2012; 7(2).

84. Tommasi D, Stock CA, Hobday AJ, Methot R, Kaplan IC, Eveson JP, et al. Managing living marine resources in a dynamic environment: The role of seasonal to decadal climate forecasts. Progress in Oceanography. 2017; 152:15–49.

85. Jacox MG, Alexander MA, Stock CA, Hervieux G. On the skill of seasonal sea surface temperature forecasts in the California Current System and its connection to ENSO variability. Climate Dynamics. 2017; 53:7519–7533.

86. Park JY, Stock CA, Dunne JP, Yang X, Rosati A. Seasonal to multiannual marine ecosystem prediction with a global Earth system model. Science. 2019; 365(6450):284–288.

87. Mogen SC, Lovenduski NS, Dallmann AR, Gregor L, Sutton AJ, Bograd SJ, et al. Ocean biogeochemical signatures of the north pacific blob. Geophysical Research Letters. 2022; 49(9).

88. Alexander MA, Scott JD, Jacox MG, Amaya DJ, Wilczynski LM. Processes that influence bottom temperatures in the California Current system. Journal of Geophysical Research: Oceans. 2025; 130(3).

89. Ito T, Deutsch C. A conceptual model for the temporal spectrum of oceanic oxygen variability. Geophysical Research Letters. 2010; 37(3).

90. Bograd SJ, Buil MP, Lorenzo ED, Castro CG, Schroeder ID, Goericke R, et al. Changes in source waters to the Southern California Bight. Deep-Sea Research Part II. 2015; 112:42–52.

91. Buil MP, Lorenzo ED. Decadal dynamics and predictability of oxygen and subsurface tracers in the California Current System. Geophysical Research Letters. 2017; 44(9):4204–4213.

92. Chikamoto MO, Timmermann A, Chikamoto Y, Tokinaga H, Harada N. Mechanisms and predictability of multiyear ecosystem variability in the North Pacific. Global Biogeochemical Cycles. 2015; 29(11):2001–2019.

This manuscript is a preprint and has not been peer reviewed. The copyright holder has made the manuscript available under a Creative Commons Attribution 4.0 International (CC BY) license and consented to have it forwarded to EarthArXiv for public posting.

93. Nam S, Takeshita Y, Frieder CA, Martz T, Ballard J. Seasonal advection of Pacific equatorial water alters oxygen and pH in the Southern California Bight. Journal of Geophysical Research: Oceans. 2015; 120(8).

This manuscript is a preprint and has not been peer reviewed. The copyright holder has made the manuscript available under a Creative Commons Attribution 4.0 International (CC BY) license and consented to have it forwarded to EarthArXiv for public posting.

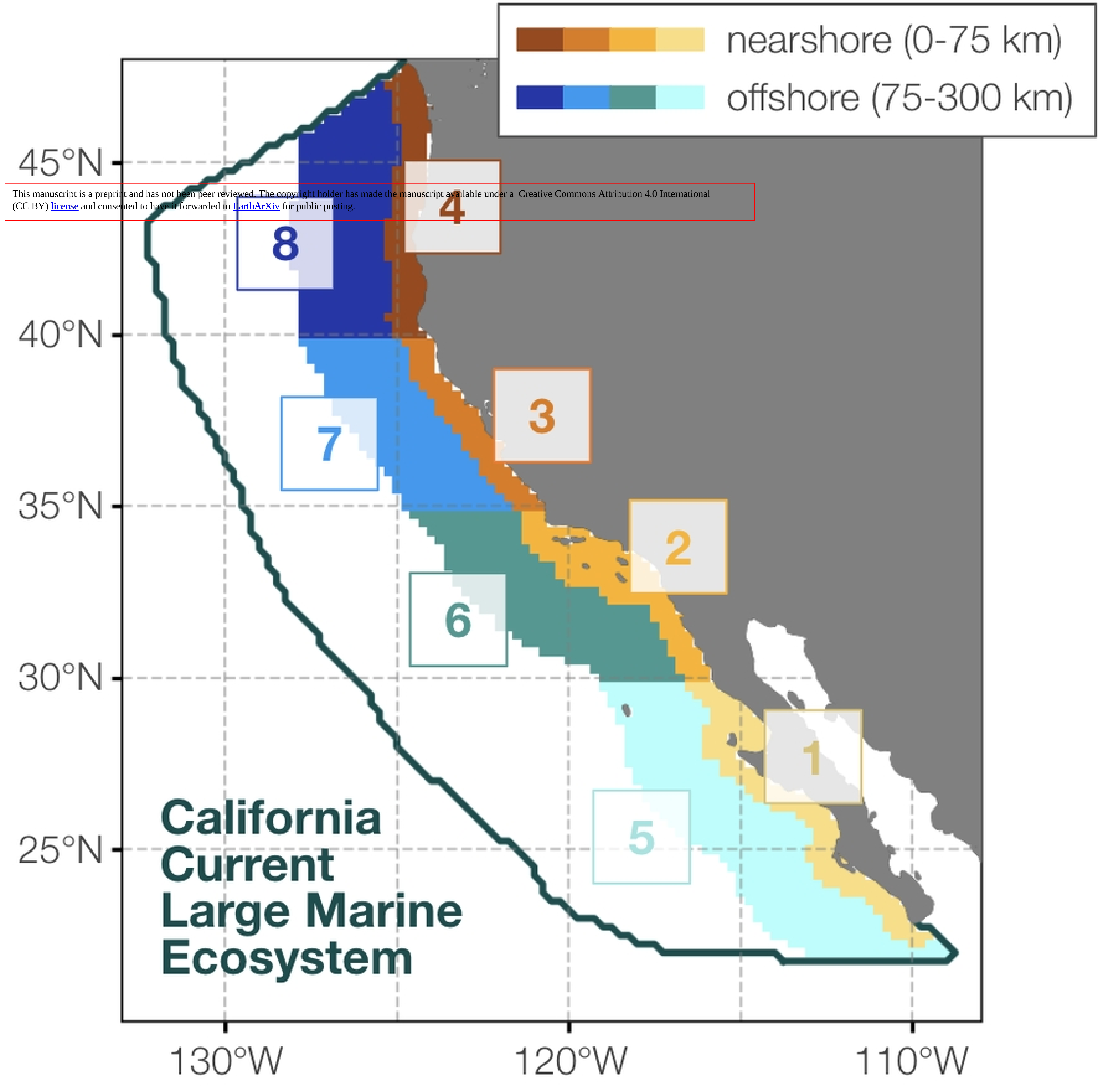

Figure 1

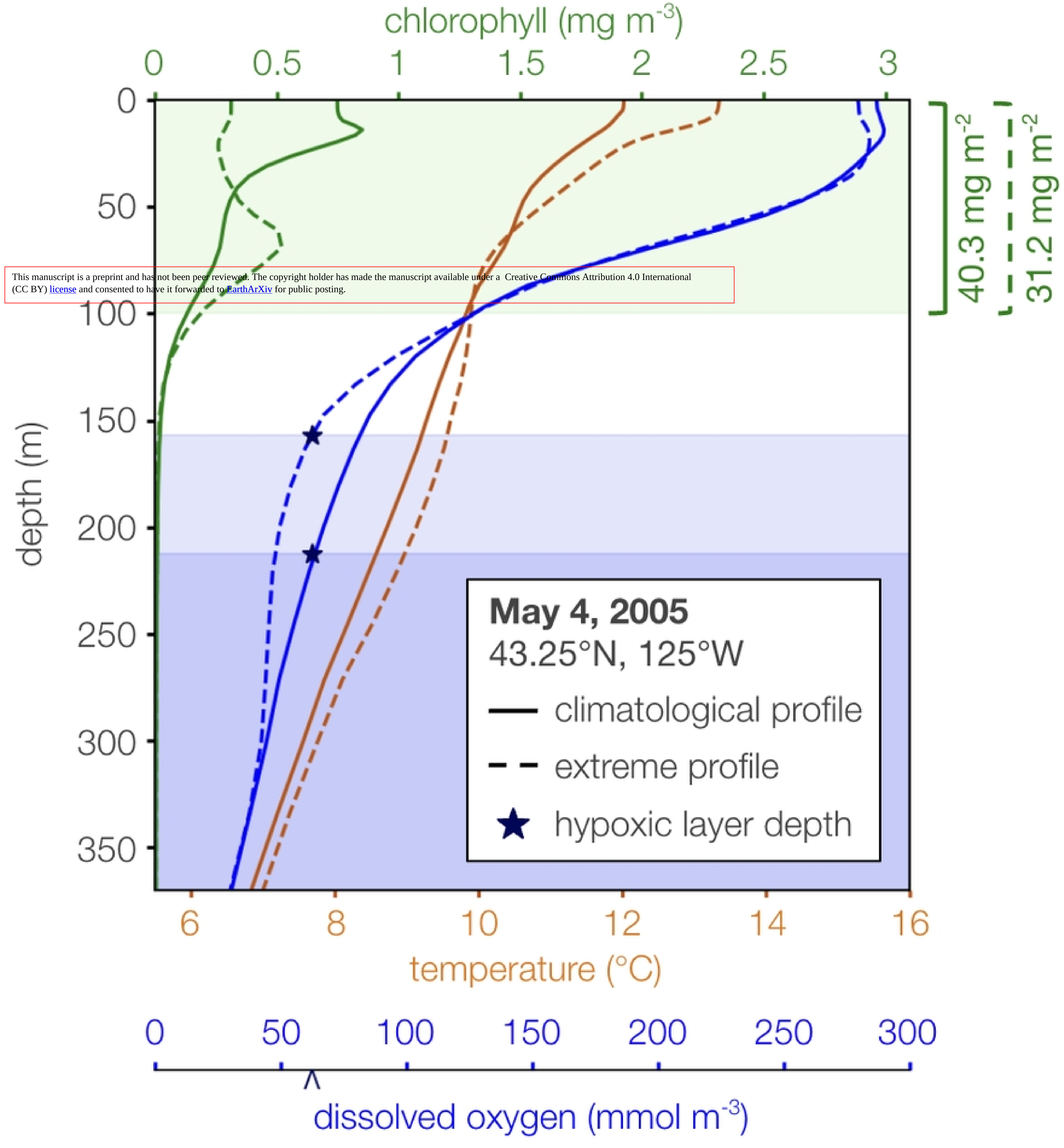

This manuscript is a preprint and has not been peer reviewed. The copyright holder has made the manuscript available under a Creative Commons Attribution 4.0 International (CC BY) license and consented to have it forwarded to EarthArXiv for public posting.

Figure 2

This manuscript is a preprint and has not been peer reviewed. The copyright holder has made the manuscript available under a Creative Commons Attribution 4.0 International (CC BY) license and consented to have it forwarded to EarthArXiv for public posting.

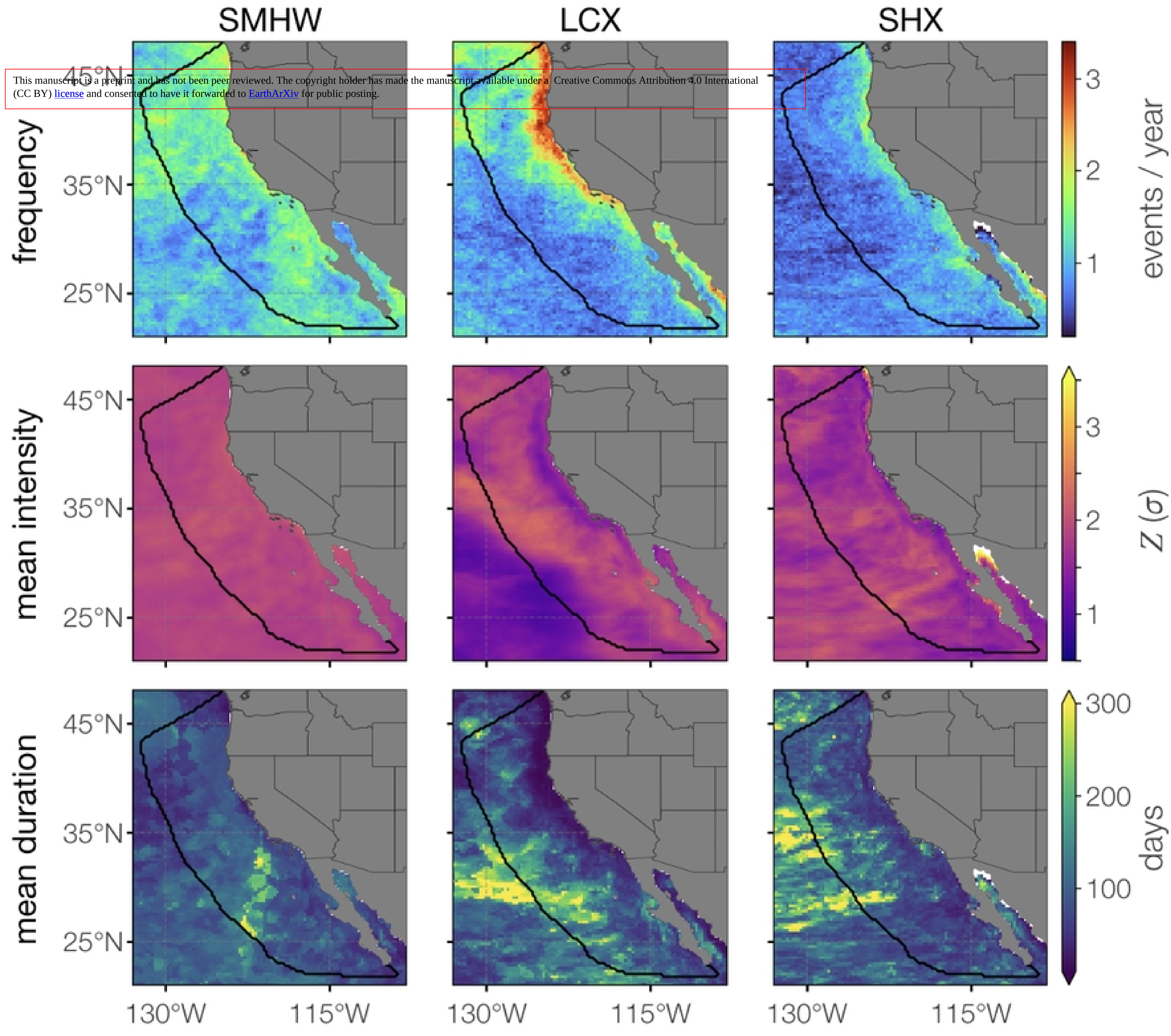

Figure 3

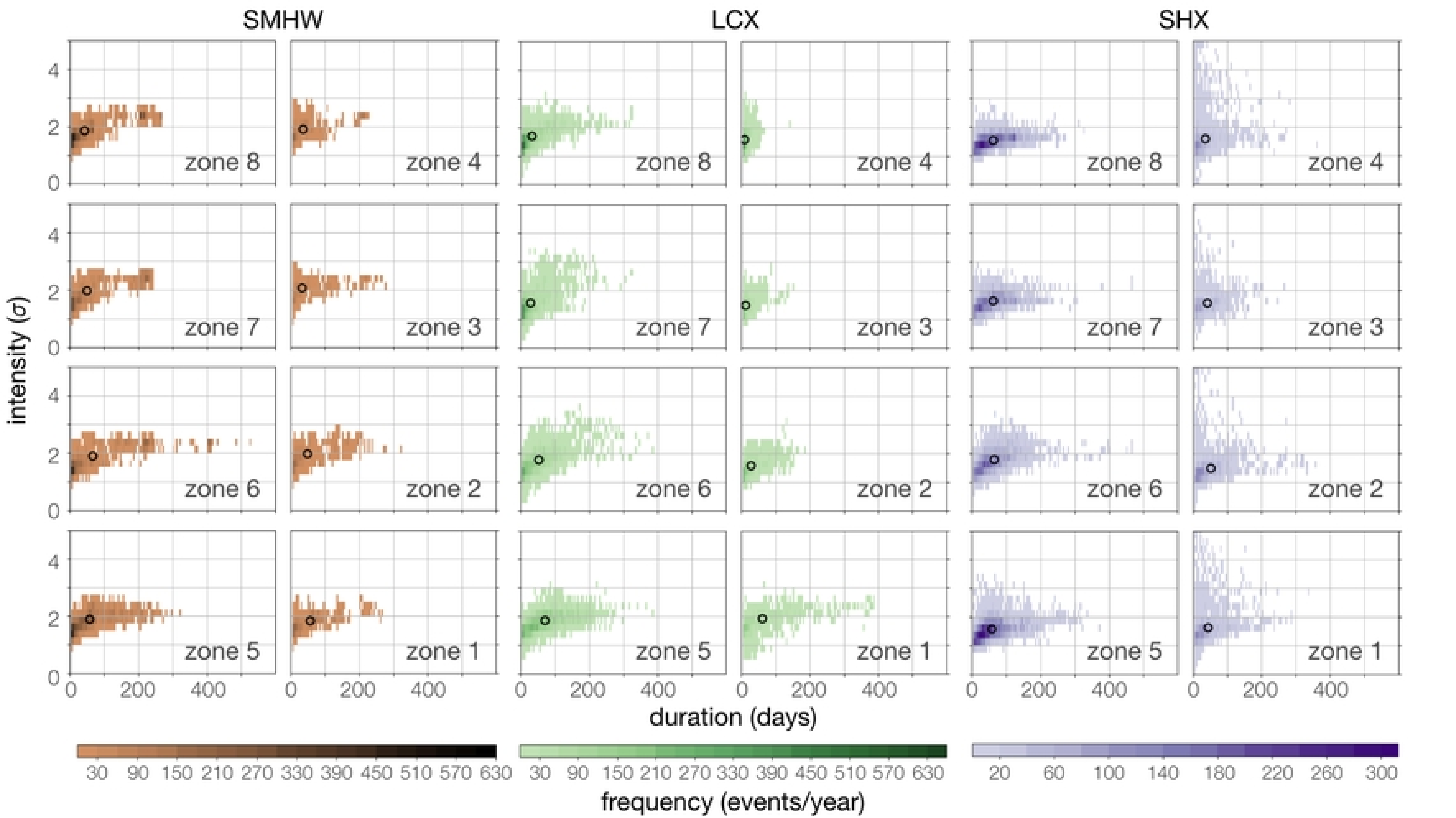

SMHW
LCX
SHX
intensity (σ)
duration (days)
zone 8
zone 4
zone 7
zone 3
zone 6
zone 2
zone 5
zone 1
0
2
4
0
200
400
30 90 150 210 270 330 390 450 510 570 630
30 90 150 210 270 330 390 450 510 570 630
20 60 100 140 180 220 260 300
frequency (events/year)

Figure 4

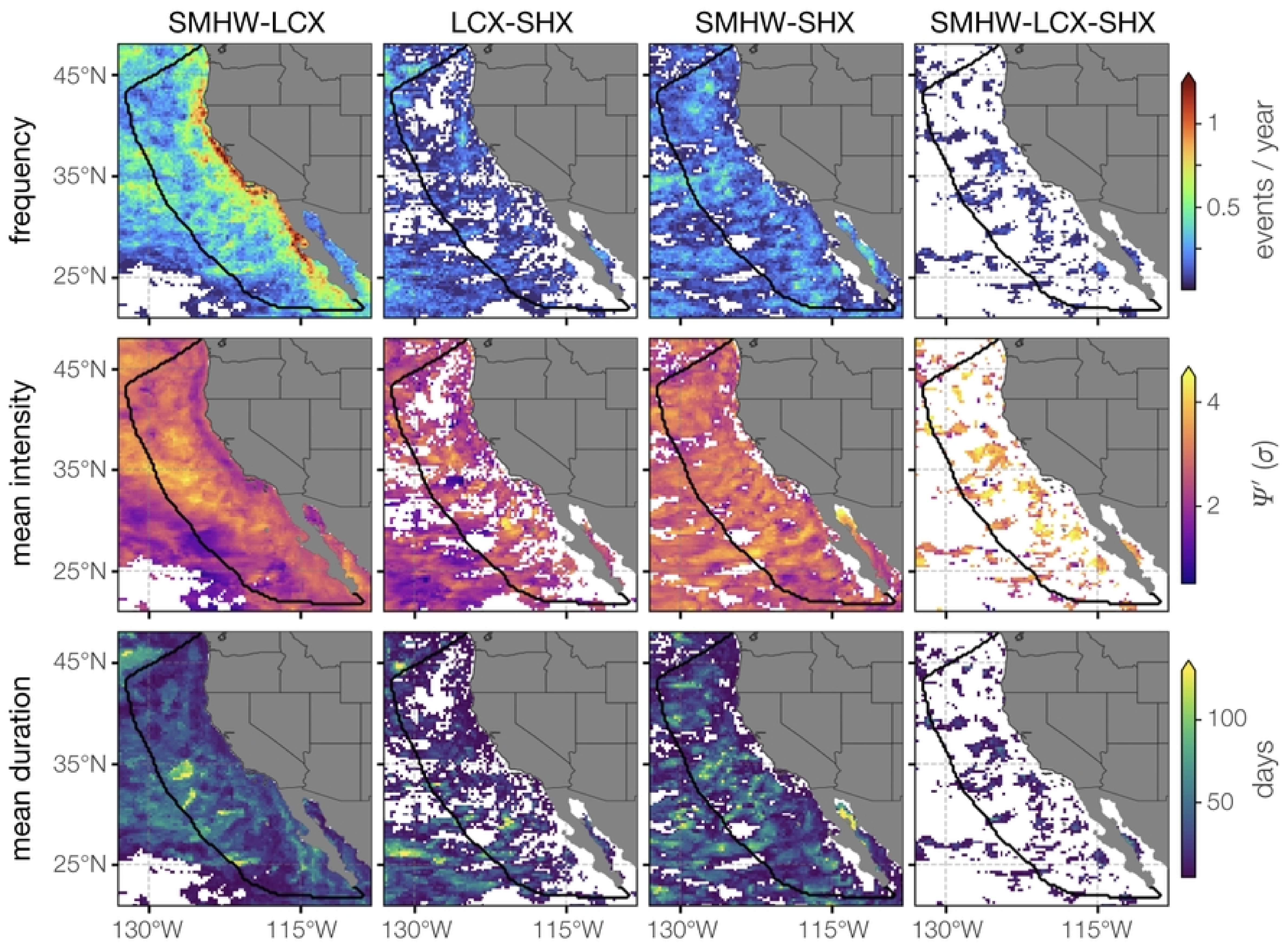
SMHW-LCX
LCX-SHX
SMHW-SHX
SMHW-LCX-SHX
frequency
mean intensity
mean duration
45°N
35°N
25°N
130°W
115°W
events / year
1
0.5
Ψ′ (σ)
4
2
days
100
50

Figure 5

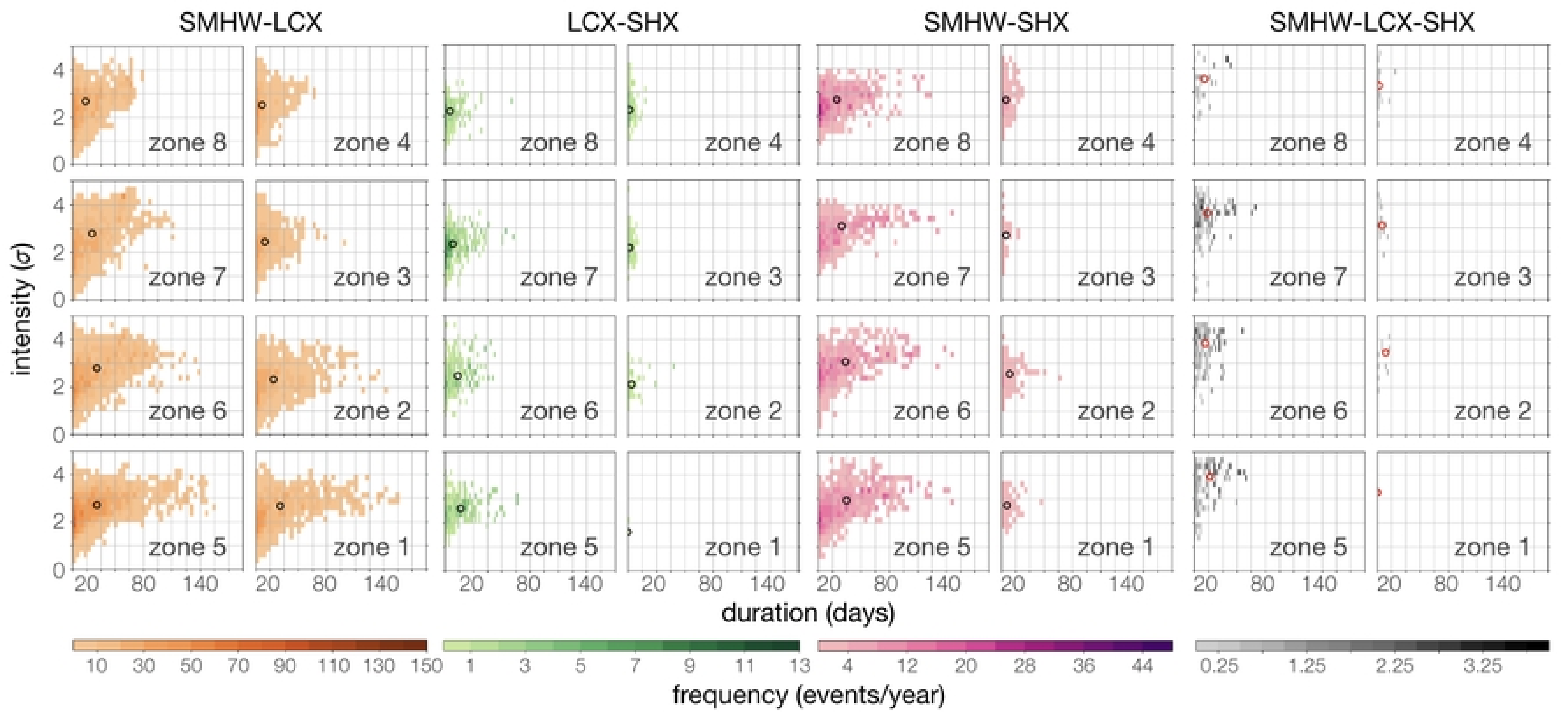
SMHW-LCX
LCX-SHX
SMHW-SHX
SMHW-LCX-SHX
intensity (σ)
duration (days)
zone 8
zone 4
zone 7
zone 3
zone 6
zone 2
zone 5
zone 1
0
2
4
20
80
140
10 30 50 70 90 110 130 150
1 3 5 7 9 11 13
4 12 20 28 36 44
0.25 1.25 2.25 3.25
frequency (events/year)

Figure 6

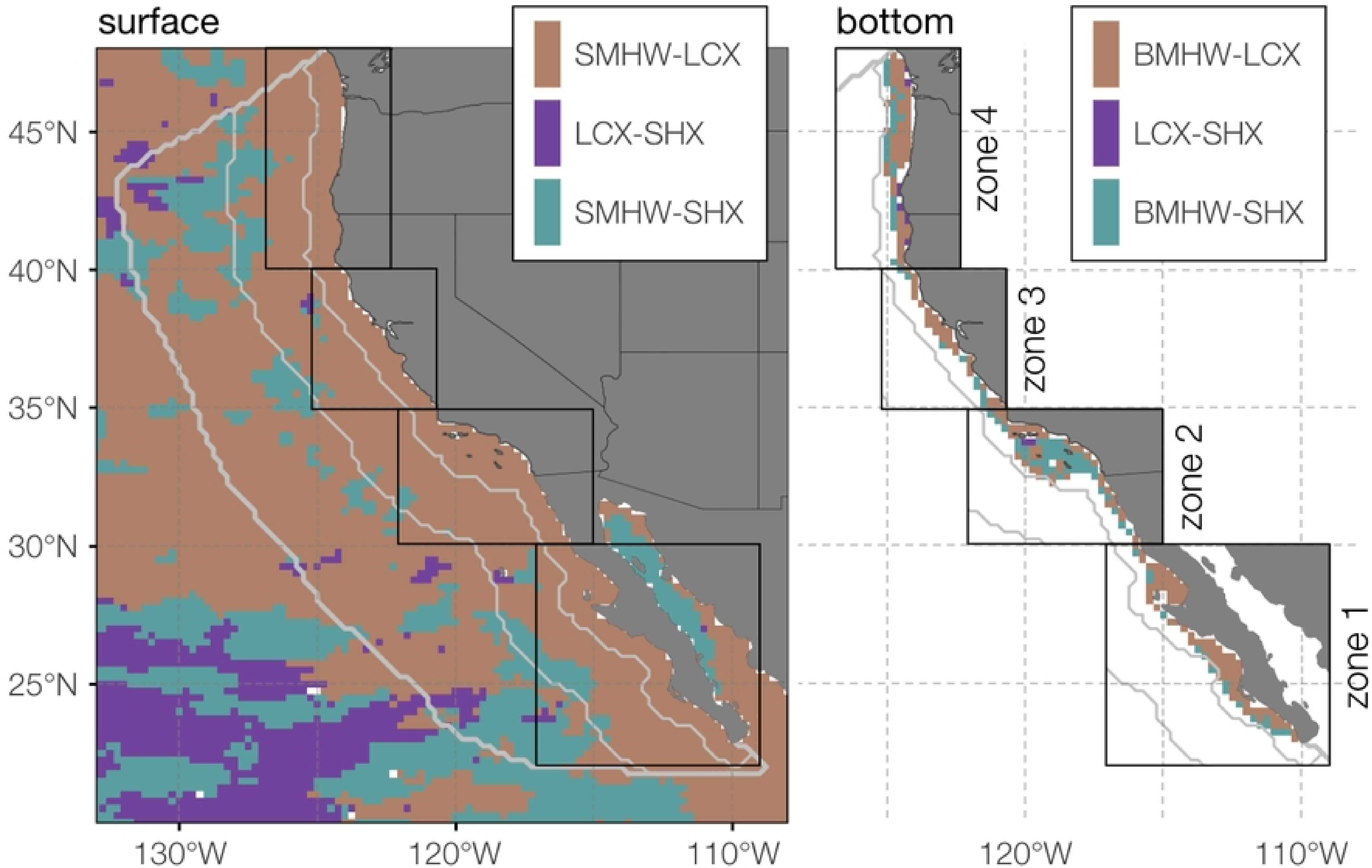

surface
SMHW-LCX
LCX-SHX
SMHW-SHX
45°N
40°N
35°N
30°N
25°N
130°W
120°W
110°W
bottom
BMHW-LCX
LCX-SHX
BMHW-SHX
zone 4
zone 3
zone 2
zone 1
120°W
110°W

Figure 7

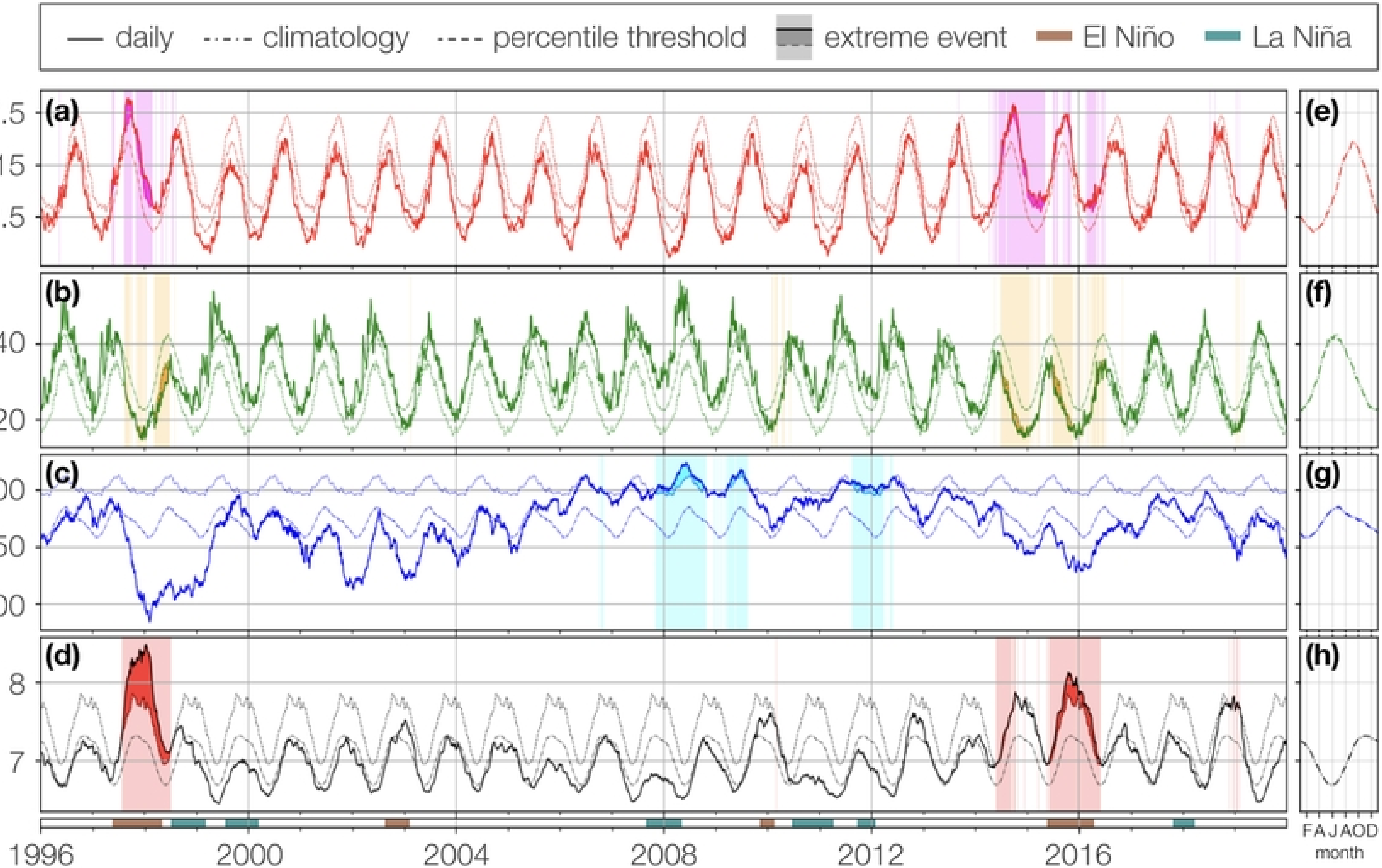

daily
climatology
percentile threshold
extreme event
El Niño
La Niña
(a)
(b)
(c)
(d)
(e)
(f)
(g)
(h)
SST (°C)
17.5
15
12.5
∫Chl (mg m⁻²)
40
20
HLD (m)
100
150
200
BT (°C)
8
7
1996
2000
2004
2008
2012
2016
F A J A O D
month

Figure 8

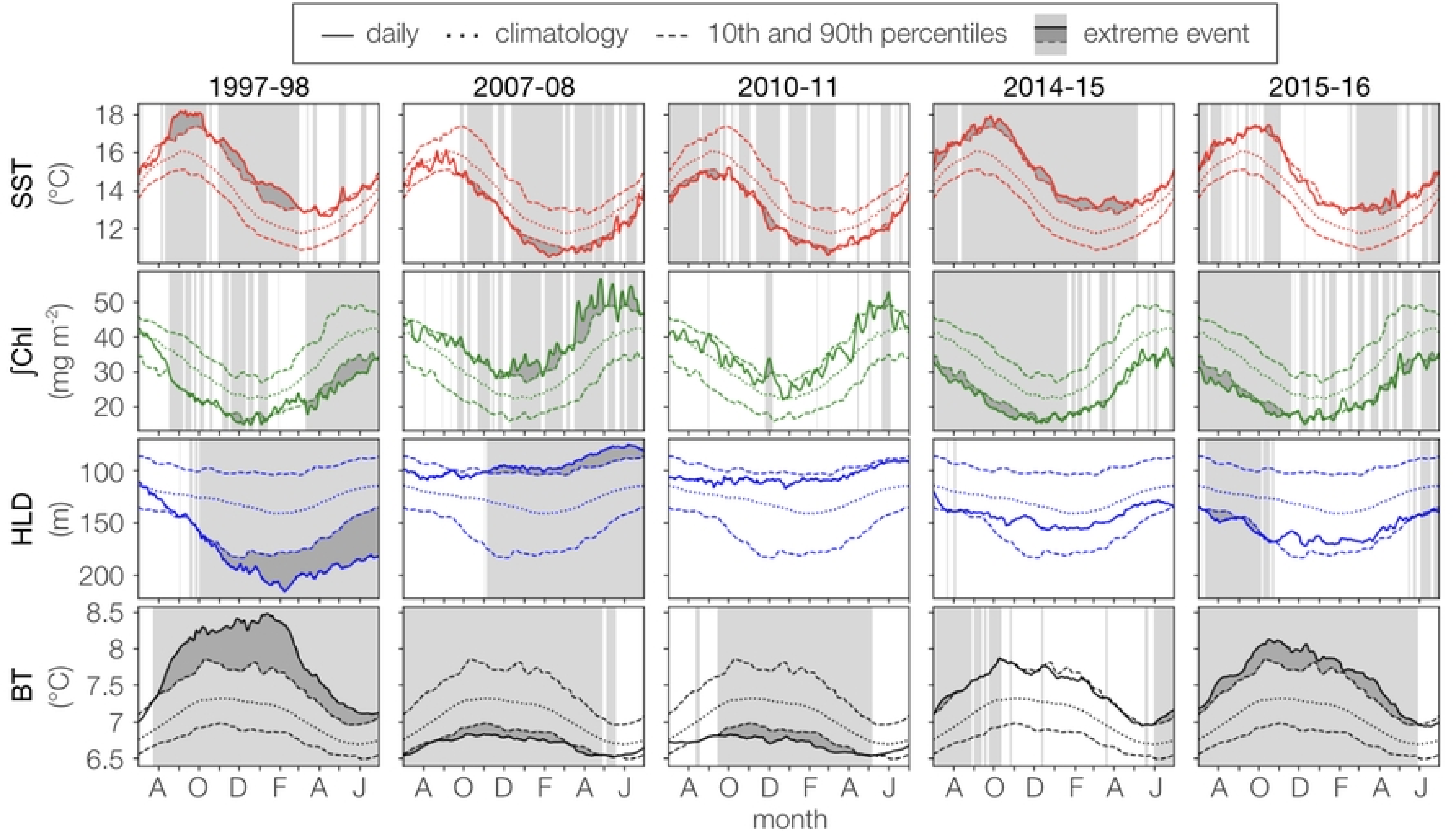

daily
climatology
10th and 90th percentiles
extreme event
1997-98
2007-08
2010-11
2014-15
2015-16
SST (°C)
18
16
14
12
∫Chl (mg m⁻²)
50
40
30
20
HLD (m)
100
150
200
BT (°C)
8.5
8
7.5
7
6.5
A O D F A J
month

Figure 9

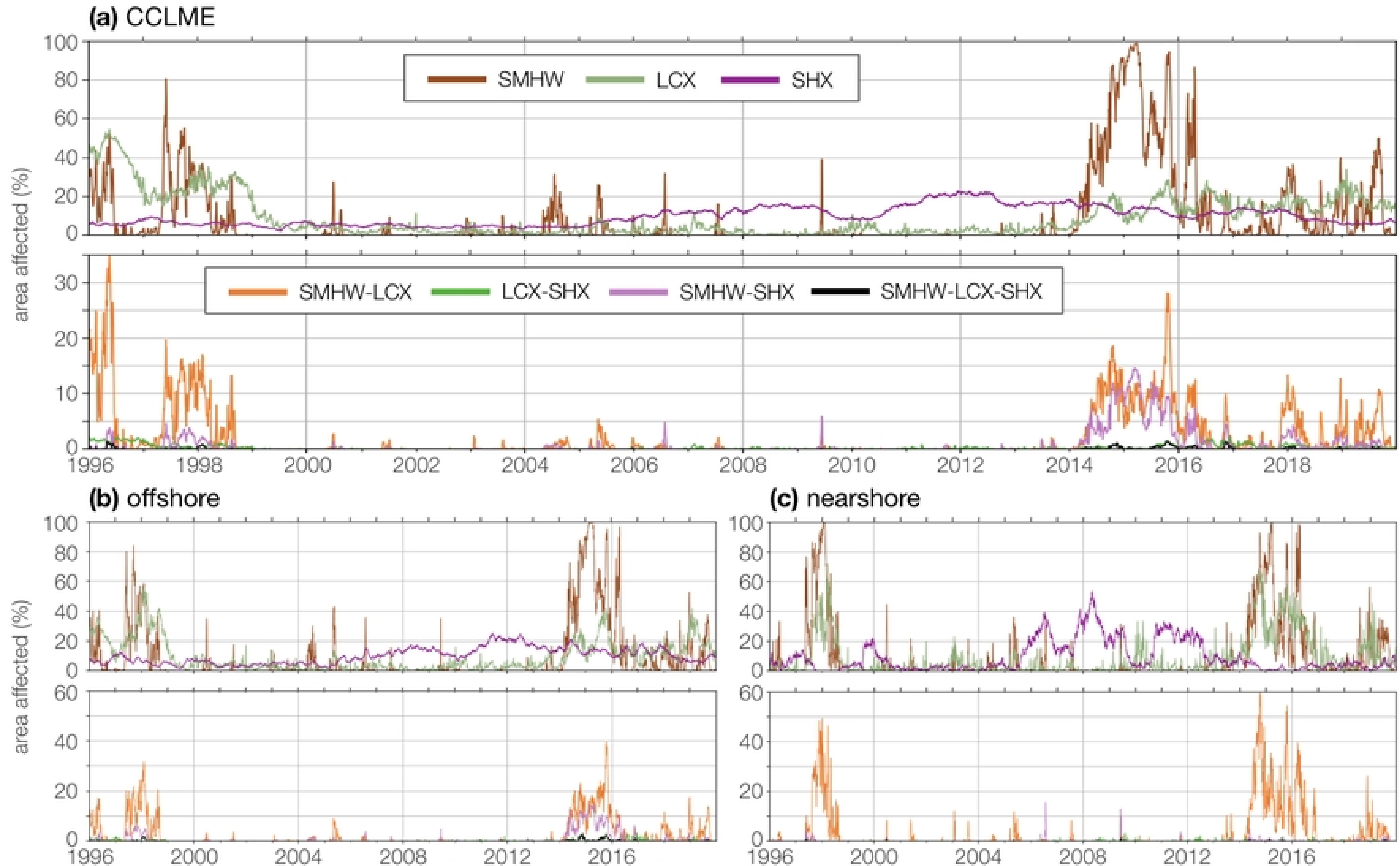

(a) CCLME
SMHW
LCX
SHX
SMHW-LCX
LCX-SHX
SMHW-SHX
SMHW-LCX-SHX
area affected (%)
100
80
60
40
20
0
30
20
10
1996
1998
2000
2002
2004
2006
2008
2010
2012
2014
2016
2018
(b) offshore
(c) nearshore

Figure 10

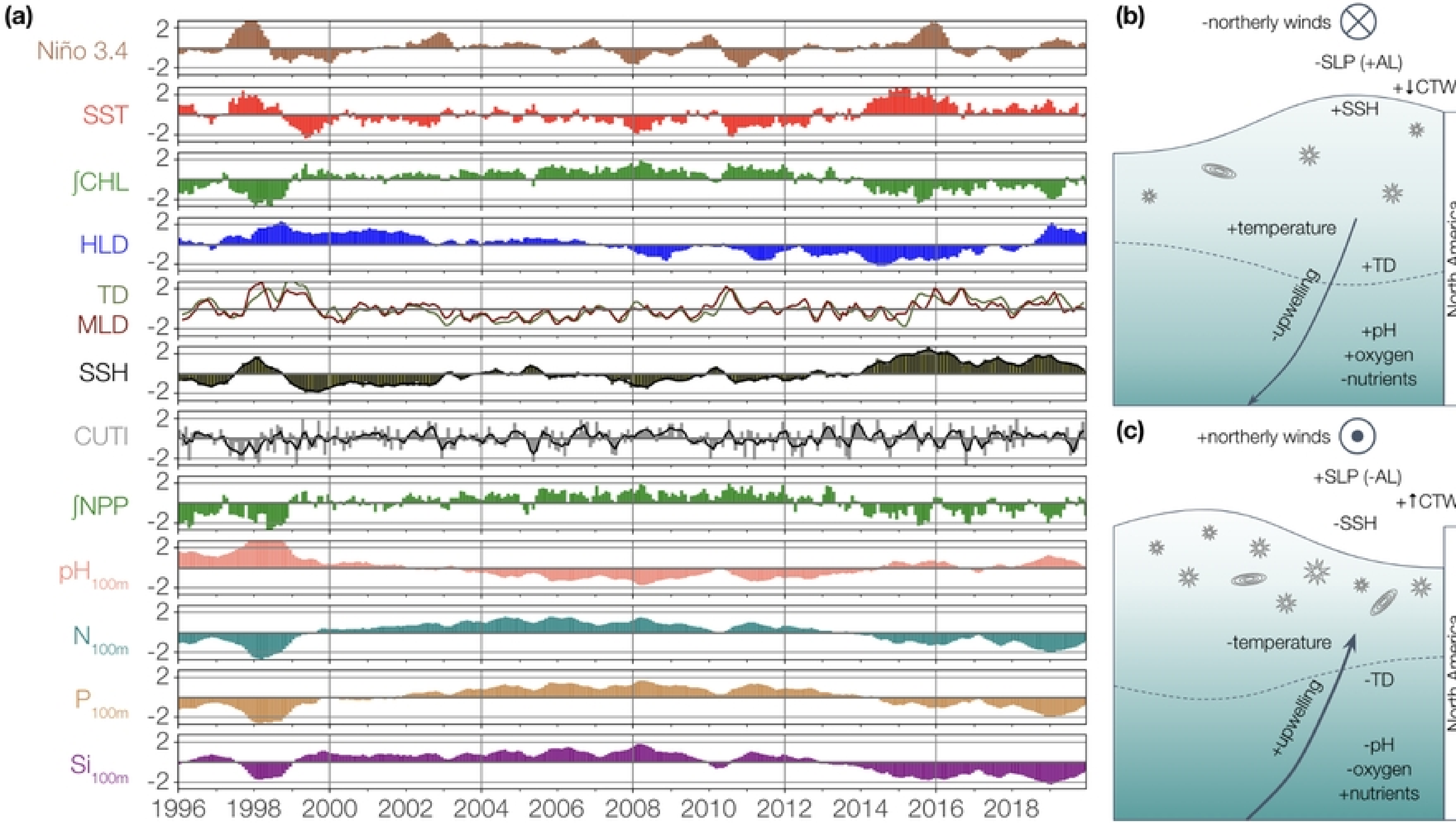
(a)
Niño 3.4
SST
∫CHL
HLD
TD
MLD
SSH
CUTI
∫NPP
pH100m
N100m
P100m
Si100m
2
-2
1996
1998
2000
2002
2004
2006
2008
2010
2012
2014
2016
2018
(b)
-northerly winds
-SLP (+AL)
+↓CTWs
+SSH
+temperature
+TD
-upwelling
+pH
+oxygen
-nutrients
North America
(c)
+northerly winds
+SLP (-AL)
+↑CTWs
-SSH
-temperature
-TD
+upwelling
-pH
-oxygen
+nutrients
North America

Figure 11